The Aftershock Sequence of the 2008 Achaia, Greece, Earthquake: Joint Analysis of Seismicity Relocation and Persistent Scatterers Interferometry

VASSILIS KARAKOSTAS,[1] KATARZYNA MIREK,[2] MARIA MESIMERI,[1] ELEFTHERIA PAPADIMITRIOU,[1] and JANUSZ MIREK[3]

Abstract—On 8 June 2008 an earthquake of $M_w6.4$ took place in the northwestern part of Peloponnese, Greece. The main shock was felt in a wide area and caused appreciable damage along the main rupture area and particularly at the antipodal of the main shock epicenter fault edge, implying strongly unilateral rupture and stopping phase effects. Abundant aftershocks were recorded within an area of ~ 50 km in length in the period 8 June 2008–end of 2014, by a sufficient number of stations that secure location accuracy because the regional network is adequately dense in the area. All the available phases from seismological stations in epicentral distances up to 140 km until the end of 2014 were used for relocation with the double difference technique and waveform cross-correlation. A quite clear 3-D representation is obtained for the aftershock zone geometry and dimensions, revealing the main rupture and the activated adjacent fault segments. SAR data are processed using Stanford Method for Persistent Scatterers (StaMPS) and a surface deformation map constructed based on PS point displacement for the coseismic period. A variable slip model, with maximum slip of ~ 1.0 m located at the lower part of the rupture plane, is suggested and used for calculating the deformation field which was found in adequate agreement with geodetic measurements. With the same slip model the static stress changes were calculated evidencing possible triggering of the neighboring faults that were brought closer to failure. The data availability allowed monitoring the temporal variation of b values that after a continuous increase in the first 5 days, returned and stabilized to 1.0–1.1 in the following years. The fluctuation duration is considered as the equivalent time for fault healing, which appeared very short but in full accordance with the cessation of onto-fault seismicity.

Key words: Aftershock relocation, PSI method, displacement field, variable slip model, 2008 Achaia earthquake.

[1] Geophysics Department, School of Geology, Aristotle University of Thessaloniki, 54124 Thessaloniki, Greece. E-mail: ritsa@geo.auth.gr
[2] Department of Geoinformatics and Applied Computer Science, AGH University of Science and Technology, Krakow, Poland.
[3] Polish Academy of Sciences, Institute of Geophysics, Warsaw, Poland.

1. Introduction

The 2008 seismic sequence (known as the Achaia earthquake) took place near the city of Patras, the third biggest city in Greece, and affected the area of northwestern Peloponnese (Fig. 1). The seismic activity there and in the surrounding area is controlled by the subduction of the oceanic crust of eastern Mediterranean beneath the Aegean microplate (Papazachos and Comninakis 1971), the impressively active Kefalonia Transform Fault Zone (KTFZ), of dextral strike–slip motion (Scordilis et al. 1985), and the back arc extension (McKenzie 1972) that constitute dominant deformational patterns in the Aegean region. The Aegean microplate is bounded to the north by the North Aegean Trough (NAT), formed by the prolongation of the dextral North Anatolian Fault into the Aegean Sea. The propagation of this dextral strike–slip motion suppressed the compressional and increased the extensional activity, with the extensional rate to be increased from 1 mm/year to about 10 mm/year in the last 1 Ma along the Corinth Gulf (Armijo et al. 1996), which is adjacent to the aftershock area (rectangle in Fig. 1).

Before 2008 the seismicity was rather low at this place (Fig. 2). Several studies were compiled for the Achaia earthquake and its aftershock sequence on the relocation of aftershocks, seismotectonic implications and deformation field. Fault surface ruptures revealed a complicated pattern comprising three main segments accommodating extensional deformation in the upper crust over a buried strike–slip fault (Koukouvelas et al. 2010), with secondary fault segments, suggesting a controversial association between ruptures and causative fault (Zygouri et al. 2015). In an immediate post-event survey Pavlides et al. (2013)
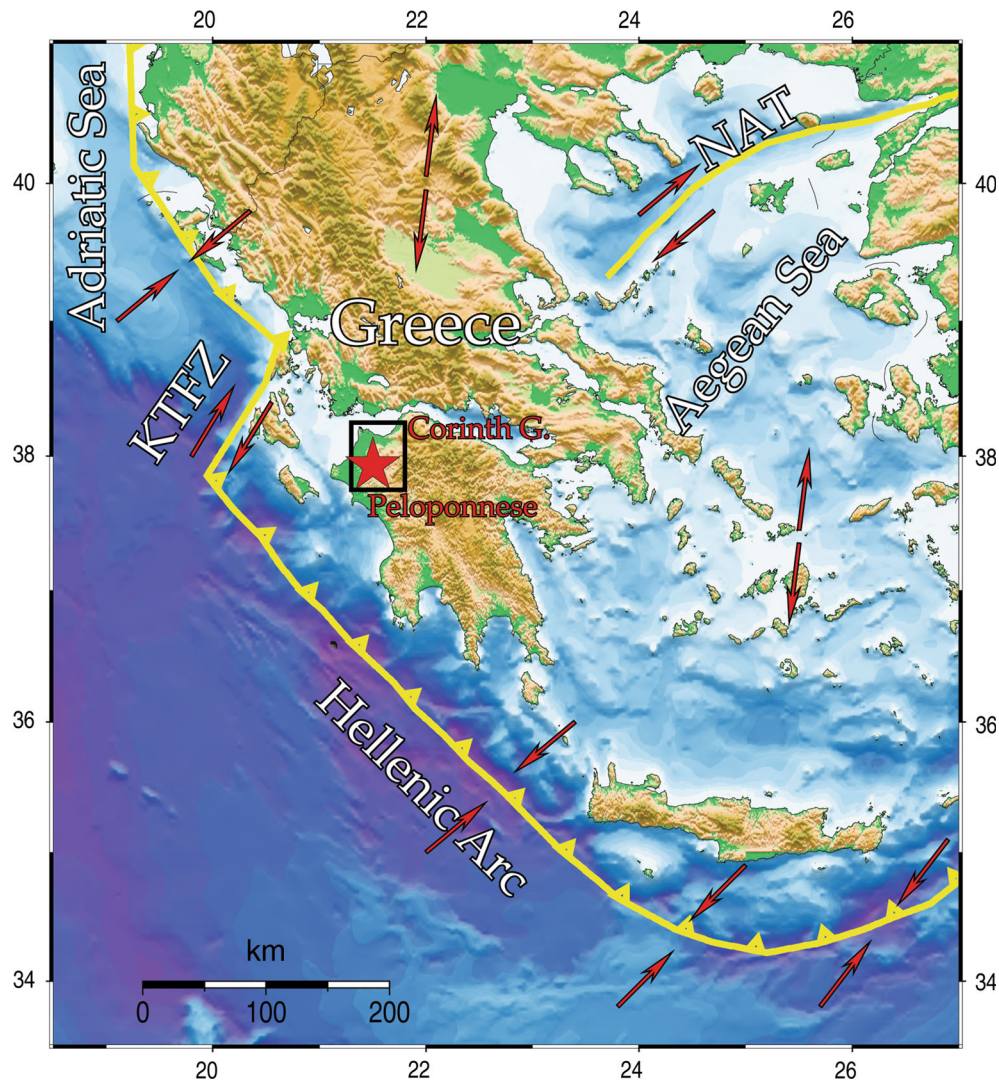
Figure 1

The Aegean and surrounding areas with the major active boundaries and the sense of relative motions. The 2008 main shock epicenter is shown by the *asterisk* inside a *rectangle* which defines our study area. *KTFZ* Kefalonia Transform Fault Zone, *NAT* North Aegean Trough

mapped in detail the distribution of the earthquake-induced ground failures, defining the areas prone to liquefaction and their associated potential. The main shock was characterized as a highly energetic rupture with $M_e \sim 6.8$–7.2, suggestive of a near order-of-magnitude increase in stress-drop over the global average (Feng et al. 2010). Directivity effects were stronger at the north end of this bilateral rupture than at the south end, manifested by 1.0 s pulses that are polarized in the fault-normal direction (Margaris et al. 2010). The differences between the estimated

fast polarization directions and the properties of the regional stress field suggest the presence of a local stress field in the area around the fault (Giannopoulos et al. 2012).

The slip evolution exhibited predominantly unilateral rupture propagation (to the north–east) along a 22-km-long fault segment with a velocity of about 3 km/s starting close to the (independently determined) hypocenter (Gallovic et al. 2009). A large slip patch (maximum slip ~ 150 cm) between 10 and 20 km depth was found at the northeast part of the
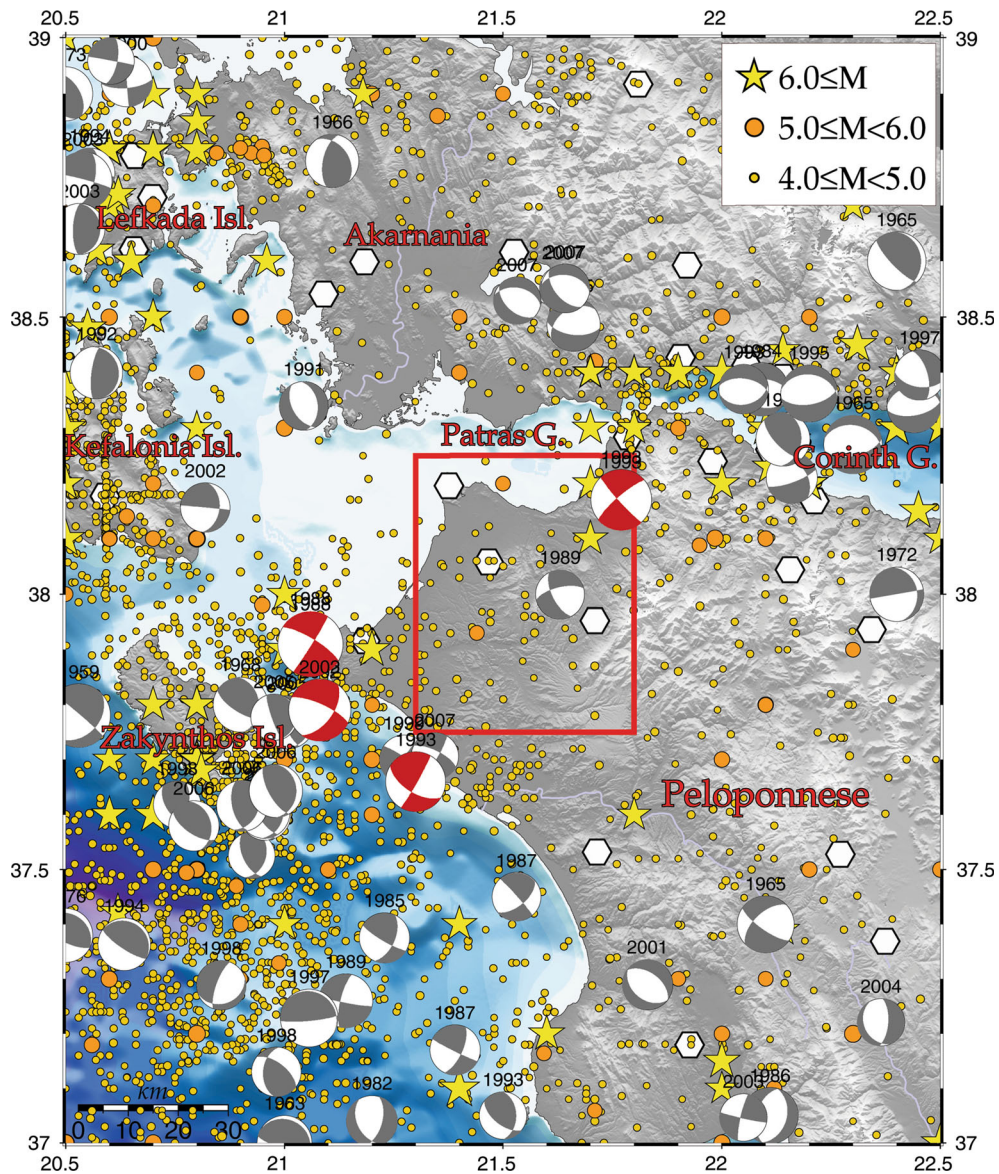
Figure 2
Map of the epicenters of the historical and instrumental seismicity up to just before the occurrence of the main shock occurrence. *Stars* depict all known earthquakes with *M* ≥ 6.0, larger *orange circles* earthquakes with 5.0 ≤ *M* <6.0 since 1911, smaller *yellow circles* with *M* ≥ 4.0 since 1970, and the smallest ones earthquakes with magnitudes M4.0–M5.9, since 2000. Fault plane solutions are shown as equal area *lower hemisphere* projections, where the ones with *red* compressional quadrants show the recent moderate magnitude earthquakes that occurred close to the study area. *Open hexagons* depict the locations of the seismological stations the records of which were used for the aftershock relocation. The study area is defined by the *rectangle*

fault that also coincides with the area that suffered most of the damage (Konstantinou et al. 2009). Similar results were found by Zahradnik and Gallovic (2010) and particularly the large time delay of the

main slip patch with respect to the origin time. Roumelioti et al. (2013) approximated the location of the fault, by trial and error and achieved the best matching between synthetic and observed amplitudes

in ground motion recordings, with the overall duration of observations better being matched when the assumed length exceeds 30 km.

Relocation of 370 aftershocks in the period of 8 June–11 July 2008 with hypoDD and 1-D velocity model was performed by Ganas et al. (2009). 438 events between 8 June until 13 July were relocated by Konstantinou et al. (2009) who used catalog and differential travel times, with most aftershocks being located in areas of low slip (<25 cm) filling the regions of slip deficit. Serpetsidaki et al. (2014) employed hypoDD and 1-D velocity model for the relocation of 872 events occurred in the first 4 months.

Historical and modern geodetic data evidenced shear consistent with the fault kinematics derived from seismological data (Stiros et al. 2013). GPS data indicate modest rates of right slip (7 ± 2 mm/year) along a southwest-trending boundary between the Northwest Peloponnesus and Akarnania (see Fig. 2 for locations) fragments (Vassilakis et al. 2011). From analysis of high-rate GPS data Ganas et al. (2009) suggested that the activated fault is part of a large, transcurrent fault zone striking NE–SW that deforms the Aegean upper plate above the subduction. From DInSAR analysis, Papadopoulos et al. (2010) stated that coseismic movement could not be detected except to a site at the northern fault edge (Kato Achaia) where vertical ground displacement of 3.0–6.0 cm was calculated, which agrees with Mirek et al. (2012). A new GPS and SAR-based deformation field was suggested by Serpetsidaki et al. (2014) and in combination with the seismological data the authors presented an updated fault model.

In this study, a larger dataset than the previous ones is used, aiming to better understand the faulting pattern in the study area, the role of stress transfer and the coseismic deformation field. Despite the comparatively high number of still ongoing publications, the location of the activated structure and the availability of seismological and geodetic data, constitute a challenge for a more thorough investigation of this sequence. A detailed earthquake catalog was compiled for a much larger period during 2008–2014, and used for delineating the rupture geometry details, temporal properties of the seismic sequence and the dominant role of stress transfer in activated area. The catalog was checked for its completeness and the complete data were used for investigating the temporal variation of the b value, seeking for an indication of fault healing. InSAR interferometry was used for detailing the coseismic deformational field and to constrain the source model. The calculated static stress field changes due to the coseismic slip of the main rupture was surveyed for evaluating the influence of this earthquake to the regional seismic hazard. Given that the 2008 Achaia earthquake is representative of past historical events and that is the only strong ($M \geq 6.0$) earthquake of the instrumental era in this area, a better understanding of the Achaia event could shed more light on the state of stress in northwestern Peloponnese, where little is known about.

2. Recent Seismicity and Faulting Properties

The area affected by the 2008 seismic excitation (rectangle in Figs. 1 and 2) is located between the fast extended Corinth rift to the north, the subduction front to the west–southwest and the Kefalonia Transform Fault Zone to the northwest. It is not included among the areas exhibiting high seismicity both during historical times and the instrumental era as it is evidenced in Fig. 2 where seismicity is plotted up to just before the main shock occurrence. For this reason, the 2008 main shock was characterized as an unexpected occurrence in most if not all the studies dealing with its occurrence. Severe damage in the city of Patras is reported (Papazachos and Papazachou 2003; Ambraseys 2009) in association with the 1785 doublet (with magnitudes equal to 6.0 and 6.5, on 31 January and 10 February, respectively), the 1804 ($M = 6.4$ on 8 June) and 1806 ($M = 6.2$ on 23 January) earthquakes, the latter being assigned to Psathopyrgos fault segment (Bernard et al. 2006; Console et al. 2013). Their approximate locations are shown by the stars close to the upper right corner of the rectangle in Fig. 2.

In the areas northeast and southwest of the 2008 rupture, moderate ($5.0 \leq M \leq 5.9$) magnitude earthquakes occurred in the last decades that produced appreciable damage in some cases and societal anxiety, mainly due to their proximity to urban areas.

Their fault plane solutions with red compressional quadrants are plotted at their epicentral locations in the map of Fig. 2. The 1988 Killini earthquake ($M = 5.9$) took place in the offshore area between Peloponnese and Zakynthos Island, fetching extensive damage in the Killini–Vartholomio area ($I_{max} = VIII$) and injury of 25 people. The aftershock sequence was studied by the recordings of a portable seismological network and found to be associated with a NNW–SSE striking fault plane (Karakostas et al. 1993a). On 26 March 1993 an earthquake of $M = 5.2$ occurred near the city of Pyrgos, to the southwest prolongation of the 2008 rupture, severely damaging at the epicentral area. Its foreshock and aftershock activity was relocated and a NW–SE striking fault was defined just beneath the city of Pyrgos, with focal depths between 4 and 26 km (Karakostas et al. 1993b). A few months later, on 14 July 1993, an earthquake of $M_w5.6$ occurred near the city of Patras, to the northwest prolongation of the 2008 rupture this time, which again caused considerable damage in the epicentral area. Its aftershock sequence was investigated using the recordings of a dense portable network (Karakostas et al. 1994). It was surprising at that time that the depths ranged between 14 and 22 km; nevertheless, the earthquake location accuracy undoubtedly supported this location of the seismogenic layer. First polarities of the local network stations revealed a NNW–SSE striking left lateral strike–slip fault with a thrust component, in agreement with the aftershock spatial distribution. The 2nd December 2002, $M_w5.5$ earthquake caused damage in the town of Vartholomio. Preliminary analysis of aftershock locations and macroseismic data support a NW–SE trending fault plane, which is connected with sinistral strike–slip motion (Roumelioti et al. 2004). The activated area seems to occupy a fault segment adjacent to the 1988 Killini segment, with similar strike.

It is worth emphasizing at this point that the occurrence of recent moderate earthquakes manifested the activation of sinistral NW–SE striking fault planes, which are in accordance with the dominant almost N–S extensional axis, dominating in the Corinth rift, and the NNE–SSW compressional axis dominating along the subduction front. The sinistral NW–SE faults seem to be the conjugate counterparts of the dominant dextral strike–slip faults comprised in the KTFZ. Sinistral motion is also evidenced to the north of our study area in Akarnania, where the 31 December 1975, $M_W6.0$ earthquake is associated with a NW–SE striking normal fault with a considerable sinistral component (Kiratzi et al. 2008). The 2008 activated dextral fault segment is bounded by the recently (1988–1994) activated smaller sinistral ones. One more evidence for the later statement are the sinistral shear strain rates on NW–SE striking structure almost orthogonal to the 2008 fault, estimated by Hollenstein et al. (2008).

3. Methods and Data

3.1. Seismological Data

The Hellenic Unified Seismological Network (HUSN) was put in operation in 2008 and the number of stations has been gradually increasing since that time. Twenty-four (24) stations were selected for the relocation, all equipped with broad band seismometers with 24 bit high-resolution digitizers, at epicentral distances up to 140 km from the center of the study area (Table 1), with P- and S-phases being recorded in a rate of 100 samples/s, at stations up to 50 km (>3000). Daily waveforms recorded between 2008 and 2014 were archived in calendar order for each station in order to use them in the cross-correlation process. All the available phases published in the monthly bulletins of the Geophysics Department of Aristotle University of Thessaloniki (GD-AUTh) and the National Observatory of Athens (NOA) were collected and used for relocating the seismicity since the main shock occurrence up to the end of 2014. The bulletins were merged and an initial catalog was compiled including 6577 events.

The magnitudes determined in the two institutions exhibited differences in the period 2008–January 2011, due to the transition from the independent networks to the Hellenic Unified Seismographic Network. In particular, from February 2008 to July 2008, the magnitudes estimated by GD-AUTh for Central Greece are 0.5 units larger than NOA magnitudes, and from August 2008 until January 2011 this difference becomes 0.1 units. Since

Table 1

Number of used P- and S-phases, and distance from the center of the study area for each seismological station

Station	N of P	N of S	Distance (km)
GUR	5238	4584	39.5
LAKA	5170	4615	27.5
KALE	5086	4441	48.0
EFP	4942	4187	47.5
RLS	4338	3964	38.5
KLV	4222	3929	23.0
DRO	3790	3619	17.5
TRIZ	3639	3053	43.0
AMT	2886	2129	54.5
VLS	2730	1899	116.5
ITM	2592	1272	91.0
DSF	2507	1805	71.0
SERG	2076	1648	48.0
UPR	1941	1506	33.0
VLX	1875	1384	82.0
ANX	1828	1277	66.0
PDO	1820	1193	91.5
PVO	1679	944	76.0
PYL	1558	494	123.0
AGG	1526	876	120.0
LTK	1469	713	93.5
EVR	1343	543	102.5
DID	1273	641	130.0
LKD2	1236	680	140.0

February 2011 both institutes are using Hutton and Boore (1987) formula after appropriate filtering of the waveforms to simulate Wood–Anderson recordings. In the present work, corrections were done by identifying a linear regression between magnitudes, taking also into account the m_b magnitudes estimated for several decades by ISC. Finally, after comparison with the available moment magnitudes they were converted to equivalent moment magnitudes.

3.2. Crustal Model

In this study more data covering longer period and with more recordings from stations in closer proximity with the aftershock area are available. Velocity models for the study area were already available (Rigo et al. 1996; Haslinger et al. 1999; Melis and Tselentis, 1998; Novotny et al. 2008) and used in the aforementioned studies for the initial aftershock location. For an improved accuracy location a new velocity model was constructed with the VELEST software (Kissling et al. 1994). Initially a $V_p/V_s = 1.79$ was estimated using Wadati plots of 135

earthquakes with more than 20 S-phases. As an a priori model the one by Melis and Tselentis (1998) was taken for locating 629 earthquakes that occurred in 2012–2014 for which more than 4P-phases were available, and have been located with HYPOIN-VERSE software (Klein 2000). The velocity model, derived after exhaustively repeating the VELEST procedure until the changes to become negligible, is shown in Table 2. Station delays from VELEST were considered as the initial ones, and a procedure of Karakostas et al. (2012, 2014) was followed for securing robustness of their final values. The new velocity model and station delays resulted in a relocated catalog of 6417 events.

3.3. Cross-Correlation

Earthquake focal coordinates were relocated using the double difference technique for securing as much as possible accuracy in the inter-event distance before cross-correlation, because waveform similarity decreases with increasing distance (e.g., Geller and Mueller 1980). The inter-event distance was reduced

Table 2

Velocity models for the study area (Rigo et al. 1996; Melis and Tselentis 1998) that were taken into account for constructing the model used for the aftershock relocation in this study

Rigo et al. (1996)		Melis and Tselentis (1998)		Current study	
V_P (km s^{-1})	Depth (km)	V_P (km s^{-1})	Depth (km)	V_P (km s^{-1})	Depth (km)
4.80	0.0	4.8	0.0	4.74	0.0
5.20	4.0	5.7	2.0	6.18	4.0
5.80	7.2	5.8	4.0	6.24	9.00
6.10	8.2	6.1	9.0	6.52	15.0
6.30	10.4	6.4	15.0	6.99	35.0
6.50	15.0	6.7	20.0	7.86	38.0
7.00	30.0	6.9	24.0		
7.90	40.0	7.2	28.0		
		7.4	31.0		
		7.6	35.0		
		7.8	38.0		

to 5 km and cross-correlation differential times were calculated for 5448 events. A time-domain cross-correlation function described by Schaff et al. (2004) and Schaff and Waldhauser (2005) was used for ~470,000 waveforms with 60 s duration starting at their origin times and having sampling rate 100 sps. Each seismogram was band-pass filtered (2–10 Hz) and updated for P and S wave readings when available. In order to avoid bias in picking from routine analysis, we applied two different windows (1 and 2 s) around the P- and S-wave picked phases and searched over a lag equal to ±1 s. The two different measurements were compared and those within 1 s with a difference in delay time lower than 0.01 s were kept. Additional criteria regarding the robustness of the cross-correlation were applied for the correlation coefficient (CC) and the number of observations in each pair. Measurements with CC ≥ 0.8 (80 %) and event pairs with 4P or 4S were kept resulting in a dataset of ~90,000 P- and ~110,000 S-phases.

3.4. Double Difference Relocation

Cross-correlation measurements were jointly inverted along with ~300,000 P- and ~200,000 S-catalog phases using the double difference technique in order to obtain the final locations. As described by Waldhauser (2001) and Waldhauser and Ellsworth (2000), the proper weighting of the data is a crucial

factor for the inversion. Twenty (20) iterations were applied using the LSQR method (Paige and Saunders 1982) along with proper damping factor after testing several values. In the first ten iterations the cross-correlation data were down-weighted by a factor of 100 in order to locate the events using the catalog data and larger inter-event distances. In the remaining ten iterations the catalog data were down-weighted by a factor of 100 in order to allow cross-correlation measurements defining structures in smaller inter-event distances. The resulting catalog consists of 5203 events with more than half of them located using cross-correlation measurements. The rest were located using catalog data only, especially in the early part of the catalog, due to the availability of fewer station recordings which resulted to lack of high-quality correlation measurements. The root mean square (RMS) of the weighted pick differential time residuals is 0.15 s, the weighted RMS of the cross-correlation data is 0.003 s, the mean horizontal error 400 m and the mean depth error 450 m.

3.5. Synthetic Aperture Radar Interferometry

Synthetic aperture radar interferometry (InSAR) is a powerful tool for imaging time-variable displacements of the solid Earth, ice and even the sea surface topography, with mm/year resolution. It is successfully used to assess coseismic deformation

(Stramondo et al. 2005; Walters et al. 2009), especially when the amount of deformation is of the order of meters. The Permanent scatterer interferometry (PSI) technique is an upgrade of InSAR and was developed to resolve the problem of geometrical and temporal decorrelation. The PSI technique uses coherent radar targets (called permanent scatterers or PS) that can be clearly distinguished in all images and do not vary in their properties. For each PS point the value of average deformation rate and coherence coefficient of radar signal are determined.

PS algorithms operate on a time series of interferogram which are formed with respect to a single "master" SAR image. There are two approaches to utilize only radar signals from stable targets. The first relies on modeling the deformation in time (Ferretti et al. 2000, 2001)—PSInSAR^{TM}, and the second one on the spatial correlation of most of the phase terms (Hooper et al. 2004, 2007)—i.e., the Stanford Method for Persistent Scatterers (StaMPS). The first approach is highly successful in urban areas, whereas the second results in better coverage, particularly in rural areas, and is also more suited for deformation, which is strongly non-linear in time. The study area is characterized by weak urbanization and is partially mountainous and for this reason the Stanford Method for Persistent Scatterers (StaMPS) is applied for processing SAR images, using DORIS software and differential interferometry.

3.6. Coulomb Stress Changes

The notion that aftershock occurrence is affected by static stress changes due to the main shock is commonly accepted (King et al. 1994; Stein 1999). Aftershock triggering is investigated here, and in particular the off-fault seismicity. The spatial correlation of the calculated Coulomb stress changes with aftershocks off the rupture surface, provides evidence that increased static stress promote failure in neighboring faults (e.g., Karakostas et al. 2003). This happens only within the distance of statistic triggering which corresponds to one or two source dimensions, the main shocks have discernible effect on subsequent seismicity (Richards-Dinger et al. 2010). The closeness to the failure was quantified by using the change in Coulomb failure function

(ΔCFF), which depends on both changes in shear, $\Delta\tau$ (computed in the slip direction), and normal stress, $\Delta\sigma$ (positive for extension), and in the presence of pore fluid takes the form:

$$\Delta CFF \quad = \quad \Delta\tau \; + \; \mu \; (\Delta\sigma + \Delta p), \qquad (1)$$

where Δp is the pore pressure change within the fault, and μ is the friction coefficient, which for the dry model ranges between 0.6 and 0.8 (Harris 1998 and references therein). In this study any time-dependent changes in pore fluid pressure are ignored and only the undrained case is considered (Beeler et al. 2000), meaning that Δp depends on the fault-normal stress whereas the fluid mass content per unit volume remains constant. Induced changes in pore pressure resulting from a change in stress under undrained conditions, according to Rice and Cleary (1976), are calculated from:

$$\Delta p = -B \frac{\Delta\sigma_{kk}}{3}, \qquad (2)$$

where B is the Skempton's coefficient, $(0 \leq B < 1)$, and $\Delta\sigma_{kk}$ indicates summation over the diagonal elements of the stress tensor. If the air fills the pores then B is nearly zero, whereas if water fills the pores, it is typically between 0.5 and 1.0 for fluid-saturated rock and close to 1.0 for fluid-saturated soil. Sparse experimental determinations of B for rocks indicate a range from 0.5 to 0.9 for granites, sandstones, and marbles (Rice and Cleary 1976). In Eq. (2) $\Delta\sigma_{kk}$ is the summation of the normal stress components, which, along with $\Delta\tau$ are calculated according to the fault plane solution of the next earthquake in the sequence of events, whose triggering is inspected. A positive value of ΔCFF for a particular fault denotes movement of that fault towards failure (that is, likelihood that it will rupture in an earthquake is increased).

4. Results

4.1. Aftershock Relocation

Figure 3 depicts the epicentral distribution of the relocated earthquakes using catalog and cross-correlation data until the end of 2014, covering an approximately 50-km elongated seismic zone,
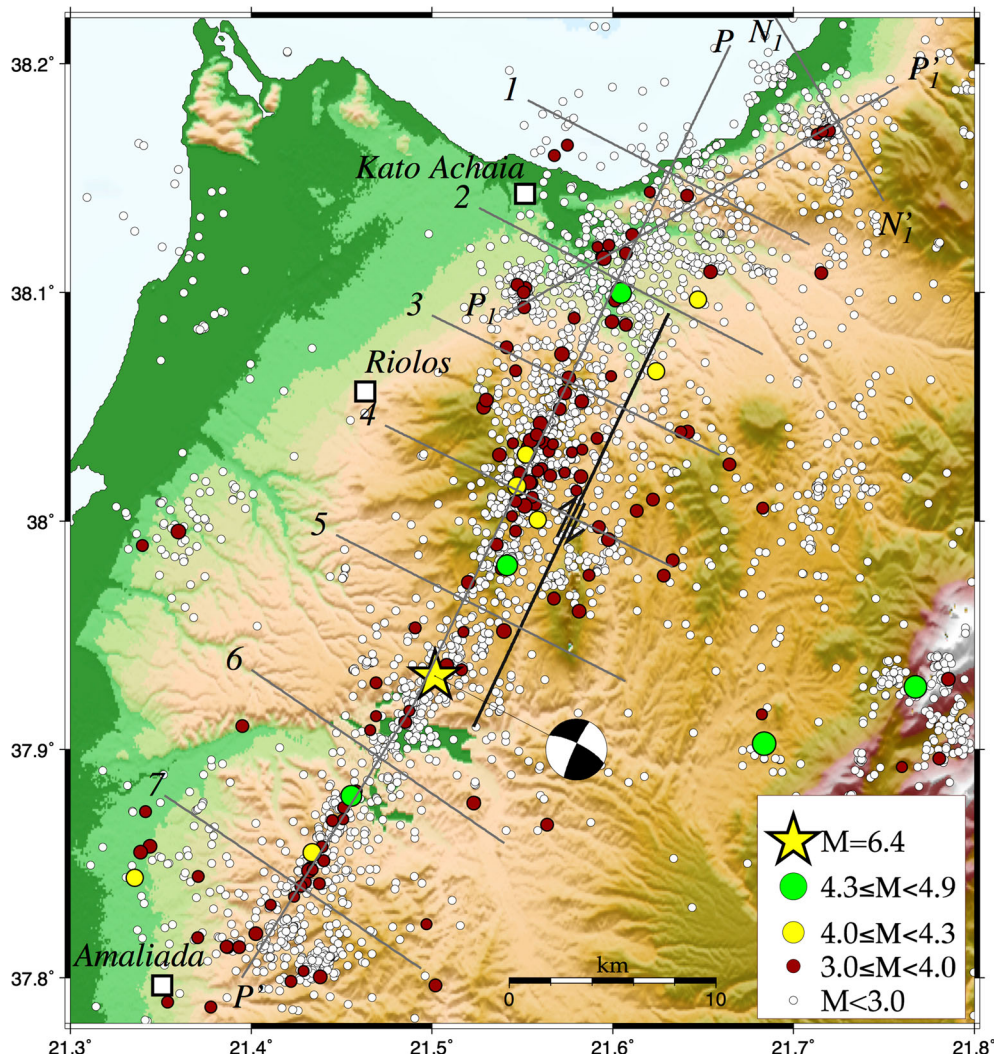
Figure 3
Map of the earthquakes that occurred in the study area since the main shock occurrence (8 June 2008) up to the end of 2014 and relocated using catalog and cross-correlation data

striking SSW–NNE in full agreement with one nodal plane of the fault plane solution. The GCMT solution, which was adopted in the present work, shows a right lateral strike–slip faulting on a high-angle dipping fault plane with slight reverse component (209/83/ 164, http://www.globalcmt.org/CMTsearch.html). This strike coincides well with the trend of the central part of the aftershock zone north of the main shock epicenter. Fault plane solutions for about 200 aftershocks were determined by Serpetsidaki et al. (2014) and are in agreement with the main shock focal mechanism. Most of the aftershocks occurred in the few months after the main shock, and their epicenters are depicted by circles of different colors increasing in size proportionally to the magnitudes (Fig. 3). The main shock is shown by a big star, and the inferred fault trace is depicted as the surface projection of the fault plane as defined by the first day aftershocks, by a black line accompanied with the antiparallel arrows expressing the dextral strike–slip faulting. The vast majority of aftershocks is of low magnitude ($M < 3.0$, open circles in Fig. 3) with very few ones
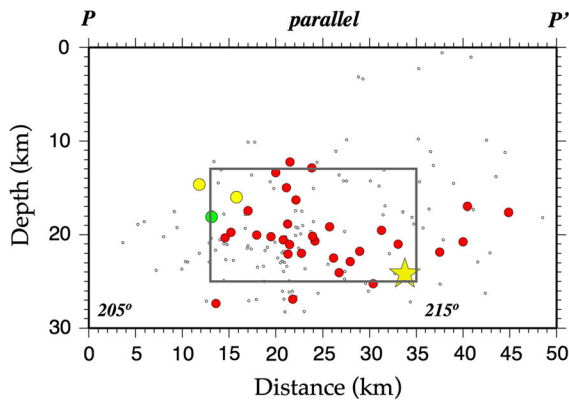
Figure 4
Strike-parallel cross section (along the line PP′ shown in Fig. 3) with the first 24-h aftershocks

Map of the relocated seismicity in consecutive time intervals, since the main shock occurrence (08 June 2008) up to the end of 2014

with $4.0 \leq M < 5.0$. The magnitude of the largest aftershock of the main rupture, which occurred in the northernmost part of the main rupture 17 min after the main shock (at 12:43 UTC, 38.0998°N, 21.6046°E) is $M = 4.3$. The magnitude difference between the main shock and the largest aftershock is then $\Delta M = 2.1$, quite higher than the globally and locally accepted average value of 1.2 magnitude units (Bath, 1965; Drakatos and Latoussakis 2001).

The investigation of the spatiotemporal evolution of the seismic activity is performed for the 6.5-year period, by constructing snapshots of aftershock epicentral distribution. The constraint of the main rupture geometry and details of the activated peripheral structures are attempted from the temporal evolution of the aftershock zone and after detailing the aftershock spatial distribution, on strike-parallel and strike-normal cross sections. The strike of the cross sections was decided after taking into account the fault strike given by the main shock focal mechanism and the dominant strike of the aftershock zone.

The first day aftershocks are plotted on a strike-parallel cross section (Fig. 4) and on a map view (Fig. 5a) for investigating the 3-D rupture extent. The section is striking at 205° to the north, while to the south after taking into account the stronger events spatial distribution (see map view in Fig. 3) its strike is taken at 215°. During the first 24 h all aftershocks with $M \geq 3.0$ but four at the southern part of the study area, are aligned close to a NE–SW striking

narrow seismicity band, in perfect agreement with the GCMT focal mechanism (Fig. 5a). It is worth noticing that the main shock epicenter is located at the southwesternmost, whereas the M4 aftershocks at the northeasternmost main fault edge, revealing unilateral rupture. The onto-fault stronger ($M \geq 3.0$) aftershocks onto the main fault are deeper than 12 km and reach the main shock depth, at 25 km approximately, thus defining the fault width along with the width of the seismogenic layer in the study area. Both the number and the magnitudes of the shallower earthquakes are considerably smaller. Inclusion of the $M \geq 4.0$ aftershocks located at the fault edge opposite to the one where the main shock is located, i.e., the rupture nucleation, results in a fault length of 22 km. This value is in agreement with what is predicted for the magnitude of the main shock according to scaling laws (Wells and Coppersmith 1994; Papazachos et al. 2004).

The temporal evolution of seismicity exhibited in the snapshots of Fig. 5 reveals that the seismic activity is clearly concentrated along and to the prolongation of the main fault segment. In the first 24 h the seismicity is impressively concentrated along a very narrow zone (Fig. 5a), implying rupture onto the main fault alone. Soon after, in the first week, the activity although continued intensively across the main fault, it also intensified beyond the fault tips, both to the northeast and southwest (Fig. 5b). It must be again emphasized that the vast majority of the stronger ($M \geq 3.0$) aftershocks are concentrated at the central part of the aftershock zone which is connected with the main rupture, and then during 2008 appear beyond both its edges (Fig. 5c). Seismicity started to diminish from 2009 onwards (Fig. 5d), without dying out completely up to the end of the study period (Fig. 5e–f).

The spatial pattern of the aftershocks distribution remains more or less the same for the next 4 years, with the magnitudes and the seismicity rate being considerably decreased in the last 2 years (2013–2014). This is an indication on the duration of aftershock sequence, which seems to last for about
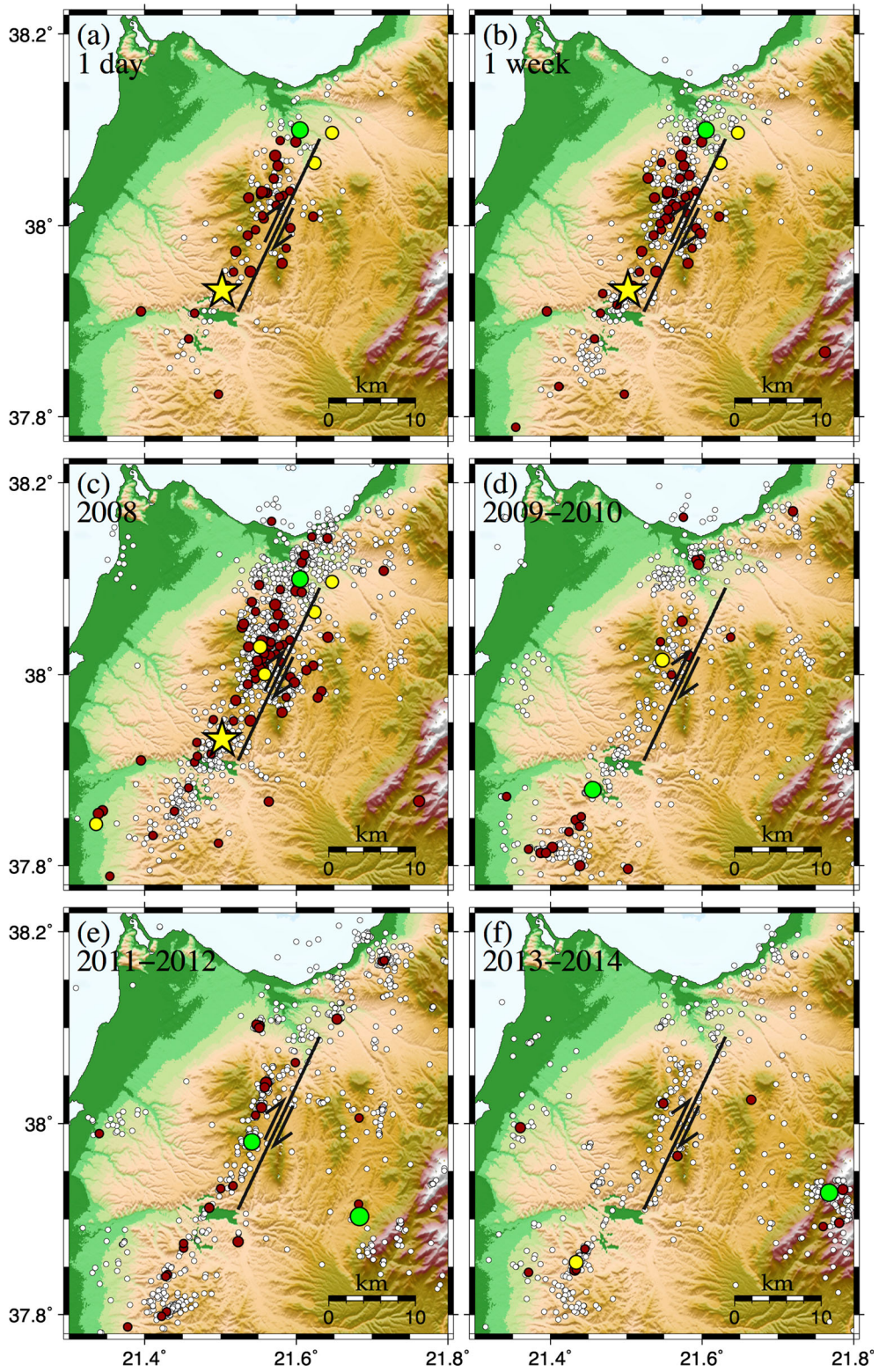
5 years (2008–2012) and then tend to decrease near to the background level. The bilateral expansion of the activity just after the first day, with small magnitude aftershocks, indicates their connection with smaller adjacent faults. At the northernmost part, northern than 38.1°N in latitude, the aftershock distribution becomes more disperse evidencing rupture on other smaller faults beyond the northern tip of the main fault, probably triggered due to the coseismic stress transfer. This aftershock activity was exceptionally intensive during 2009–2010 and continues up to the end of 2014, forms an ∼20 km long and WSW–ENE striking zone of about 60°, considerably different than that of the central part, which is the area of the main fault. Activated minor fault segments but NW–SE striking were also identified at the same area by Serpetsidaki et al. (2014). The

seismic activity beyond the southern tip of the main fault includes low magnitude earthquakes alone, and exhibits a slight change in the trend to NNE–SSW manifestations of seismicity bursts, which is a common phenomenon in the study area, and a couple of them are discernible in the maps of Fig. 5.

For detailing the geometry not only of the main rupture but also of the secondary ones, a number of cross sections were constructed (Fig. 6). A strike-parallel cross section (along the line PP′ in Fig. 4) includes the earthquakes with hypocenters in a zone of 10 km either side of the cross section. A different strike (215°) was chosen for the cross section of the earthquakes south of the main shock as evidenced from the $M \geq 3.0$ earthquakes in this area. The inverse triangles on the top show the positions of the strike-normal sections. The rectangle, showing the
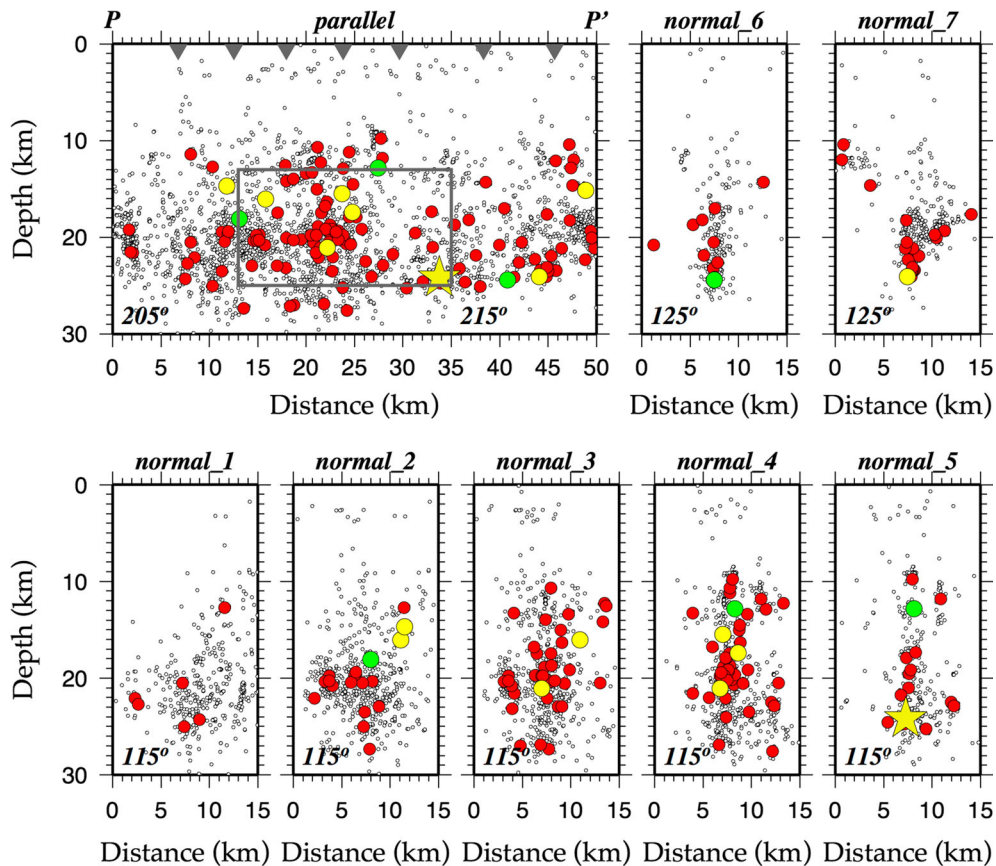

Figure 6
Strike-parallel and strike-normal cross sections of the aftershock zone, the positions of which are shown in Fig. 3. The inverse triangles on the top line of the strike-parallel section mark the strike-normal sections

main fault segment, comprises most of the $M \geq 3.0$ earthquakes during the entire study period. Fewer aftershocks close to the main shock location imply the existence of a maximum slip fault patch. Smaller magnitude events are located close to the surface, at depths shallower than 4 km. Most probably these are mislocated shocks due to errors in the phase picking caused by presence of noise or other incidental reasons. Although the thickness of the seismogenic layer is not everywhere the same as the strike-normal cross sections reveal, the brittle part of the crust is confined at depth ~ 12–27 km, comparatively deeper than in other cases of the back arc Aegean area (e.g., Karakostas et al. 2014).

The first two strike-normal cross sections (normal_6 and normal_7 in Fig. 6) comprise aftershocks in a band of 4 km either side of the lines shown in Fig. 3, which occurred south of the main shock epicenter, and reveal an active structure with a strike of about ten degrees difference of this part in comparison to the north. The small magnitude earthquakes evidence triggering of smaller fault segments along this southward prolongation of the aftershock activity. Although the stronger ($M \geq 3.0$) aftershocks occur at depths between 12 and 27 km, similarly to the northern part, the vast majority of them define a seismogenic layer that is confined between 17 and 25 km. The hypocenters define a thin vertical seismic zone (normal_6) and in the southern most part (normal_7 and strike-parallel cross sections) the existence of probably other small faults with different geometry. This activity started in the first day of the seismic sequence and continued persistently with low magnitude shocks.

The five next cross sections in Fig. 6 (from 1 to 5) have the same orientation (115°) normal to the trend of the main rupture, and as before, encompass data at a distance of 4 km either side of their surface projection. In the two strike-normal northernmost profiles (normal_1 and normal_2) hypocenters are mainly confined at depths 19–25 km, whereas in the next three (normal_3, normal_4 and normal_5) in between 11 and 27 km, forming a zone dipping at a very high angle to the WNW.

A 60° trending vertical cross section (along the line P_1P_1' shown in Fig. 3) is presented in Fig. 7a, encompassing the hypocenters of earthquakes located

northern than 38.09°N. The most characteristic feature in this cross section is a cluster in the northeastern part of the zone, comprising several hundreds of microearthquakes. The cluster has a length of about 2 km and a width of 3 km. A normal cross section (Fig. 7b) manifests a thinner horizontal dimension (less than 1 km) supporting that this cluster is associated with a small fault striking in a WSW–ENE direction.

4.2. Persistent Scatterers Technique

In this study we used ENVISAT data acquired by the European Space Agency (ESA), 13 scenes totally from track 186, spanning the interval from 19 February 2006 to 19 April 2009, and covering the north–west part of the Peloponnese (http://www.nr-can.gc.ca/earth-sciences/geomatics/satellite-imagery-air-photos/ satellite–imagery–products/educational–resources/9325). The image from March 30th 2008 was selected as a reference one. In the first stage the DInSAR technique was used to study the coseismic deformation. The external DEMs (Digital Elevation Model) were used in coregistration of selected pair of SAR images to increase precision. To assess the exact SAR sensor position the precise satellite orbit state vectors provided by ESA DORIS system were used. However, only one pair (2007.12.16 and 2008.07.13) gave satisfactory results. Although there were sets of fringes visible in Kato Achaia area, accurate deformation estimation was not feasible. The interferogram shows line-of-sight (LOS) ground movement of about one to two fringes, which is approximately LOS uplift from 2.8 to 5.6 cm, also mentioned by Papadopoulos et al. (2010).

Generally interferograms were highly decorrelated. The temporal decorrelation is one of the most important factors that cause problems in interferogram analysis and interpretation. The study area is characterized by weak urbanization, and this probably resulted to the substantial temporal decorrelation observed in the interferograms. Decorrelation could be also attributed to steep local topography. Given that it is also partially mountainous, in the second stage the Stanford Method for Persistent Scatterers (StaMPS) for processing of SAR images was used. StaMPS is the software that leads to reliable results
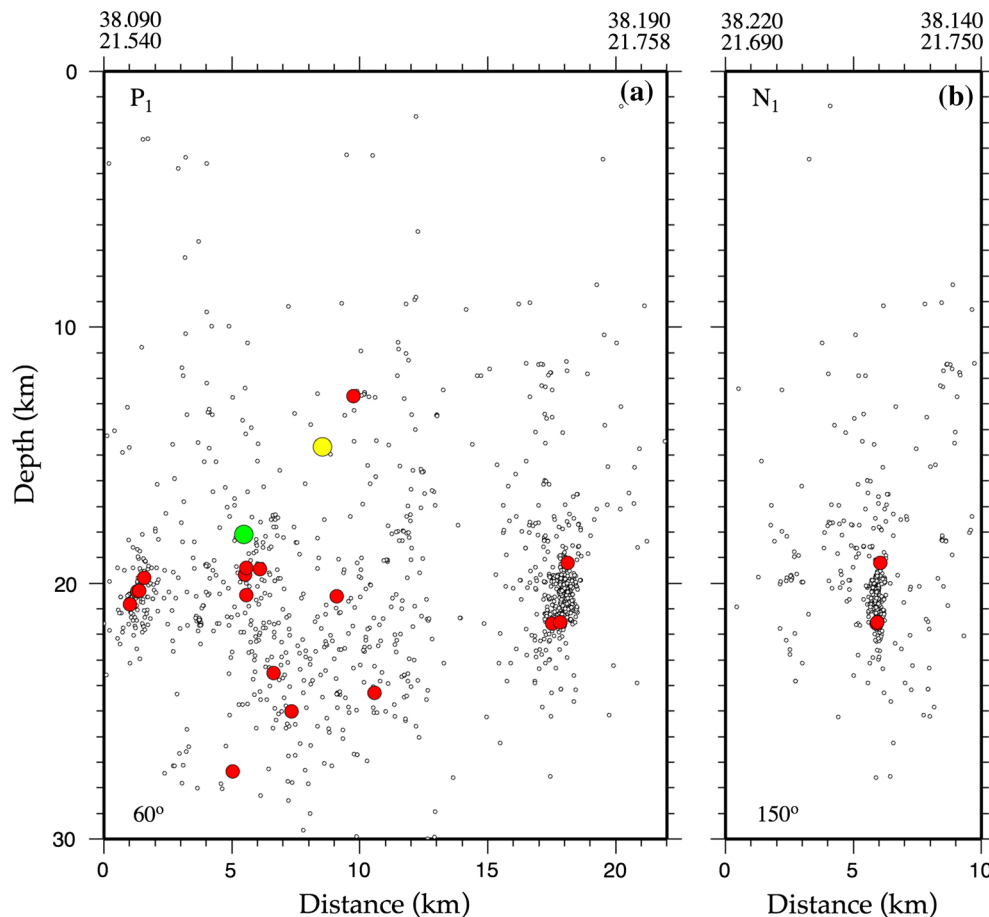
Figure 7
Strike-parallel and *strike-normal* cross sections of the northern cluster (along the lines P_1P' and N_1N', respectively, shown in Fig. 3), beyond the northeastern tip of the main fault

even in terrains devoid of man-made structures. The end product of the processing is a map of coseismic deformation, projected into the line-of-sight (LOS) of the observing satellite. The number of stable-phase pixels equals to 75,209. Information on PS points deformation was used to construct the coseismic deformation map (Fig. 8). The field displacement reveals that the coseismic deformation is concentrated in "patches" around the fault: uplift is visible in north–west and south–east near the fault edges, and subsidence at the south–west and north–east. Although the latter is characterized by lower values, it is distinct throughout the northeastern quadrant of the area surrounding the fault.

One station of a continuous GPS network maintained by the National Observatory of Athens (NOA) is located at the village of Riolos (to the NNW of the main shock epicenter of Achaia earthquake, green hexagon in Fig. 8). The coseismic displacement observed on this station is 10.53 ± 0.85 mm in the vertical component (uplift) (Ganas et al. 2009). Figure 9 shows a time series plot of LOS velocity displacement for PS points near this station, whose position is shown by the hexagon and where the mean rate of surface uplift is ~ 7.5 mm, less than the measured value; however, the scattering should be taken into account.

4.3. Slip Model and Displacement Field

The aftershock distribution supports a main rupture on a rectangular plane with a length of 22 km and width of 12 km, respectively, as it was
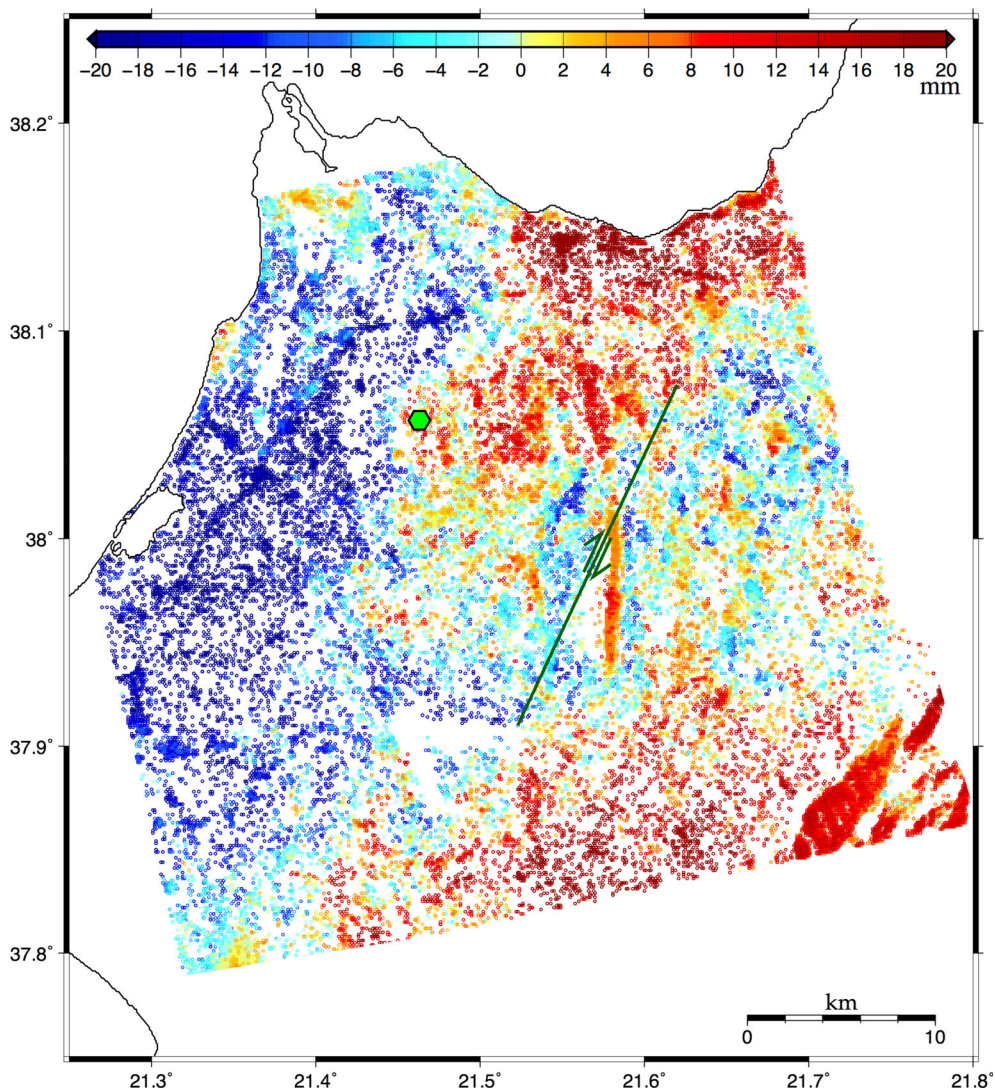
Figure 8
Surface deformation map (in LOS direction) for coseismic period, calculated by the Stanford Method of Persistent Scatterers (StaMPS). The fault is marked as a *solid green line*, GPS station RLS is marked as a *green hexagon* and *color bar* is in mm, where the positive values imply uplift

already mentioned in a previous section. It concerns a plane dipping at high angle in agreement with the GCMT solution and several published fault plane solutions for earthquakes close to our study area. The aftershock spatial distribution designated a mean strike of 205° for the main rupture, which is in excellent agreement with the GCMT solution (209°) and is assigned to the coseismic rupture model. The dip and rake were adopted from this solution, as 83° and 164°, respectively. Taking into account the seismic moment $M_o = 4.56 \times 10^{25}$ dyn cm, the

rigidity value $\mu = 33$ GPa, and according to the relation $M_o = \mu \cdot u \cdot L \cdot w$ a mean slip $u = 0.52$ m homogeneously distributed onto the fault plane was estimated. The resulted surface displacements from this rectangular dislocation plane with the above characteristics were calculated using the Okada's (1992) equations and the Dis3dop program (Erikson 1986) software.

Calculations with a homogeneous slip resulted in an overestimation of the displacement field, as they were presented in the aforementioned studies of
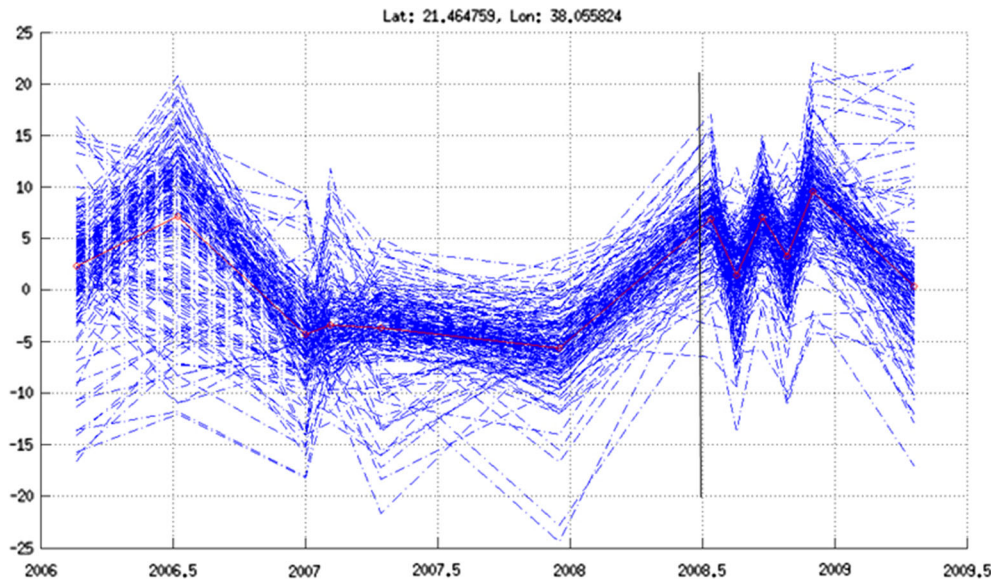
Figure 9

Time series plot of surface deformation for PS points near the GPS station located at Riolos (RLS). *Vertical solid black line* is drawing approximately at the main shock occurrence time. The *red line* is the mean displacement rate from all PS points

Ganas et al. (2009) and Serpetsidaki et al. (2014) for GPS and InSAR measurements. This provides a first evidence that the major amount of slip was released from deeper patches of the rupture area. The fault plane was then divided into equal area square cells (2 km × 2 km) where slip values equal to 0.13, 0.26, 0.39, 0.52, 0.78 and 1.00 m were assigned ($\sim$0.25, 0.5, 0.75, 1.0, 1.5 and 2 times, respectively, the mean slip value), integrated to a total fault area that maintains the seismic moment value constant. The position and the dimensions of the fault plane are those determined by the first day aftershock spatial distribution (Figs. 4, 5a). The proposed variable slip model shown in Fig. 10 approaches the geodetic observations better than a model of constant slip and several others with variable slip that were tested, and for this reason it was preferred. A color scale and arrows show the movement of the hanging wall onto the footwall surface, which appears in this figure. The upper part of the model (13–19 km), requires low slip, whereas in the depth range 19–25 km considerably higher slip is required. The maximum slip patches occupy the base of the seismogenic layer, the one around the nucleation point and the second at the northern part. The predominant slip occurred near the

main shock hypocenter and at the SSW edge of the rupture area, with a maximum value of $\sim$0.8–1.0 m, at depths 21–25 km. This high slip patch occupies the deeper part of the northwestern patch, as the one suggested by Konstantinou et al. (2009), although their patch is located in between $\sim$10 and 15 km. The mean slip value is suitable for the shallower rupture part, approximately to 15–20 km in depth.

The calculated surface displacement field resulted from this model is shown in Fig. 11. The horizontal displacement components are depicted by the grey arrows with lengths according to the scale shown at the lower right part of the figure. Uplift and subsidence are denoted by contours of positive and negative values, respectively. For a better visual inspection yellow to red values denote uplift and blue shades represent subsidence. In the same figure the observed horizontal displacements with their uncertainties, as published by Serpetsidaki et al. (2014), were plotted by black arrows. The respective values calculated with our model at the observation points were plotted by white arrows. At the only location indicated by the hexagon (Riolos), where both vertical and horizontal displacements are available (from Ganas et al. 2009), approximately equal to
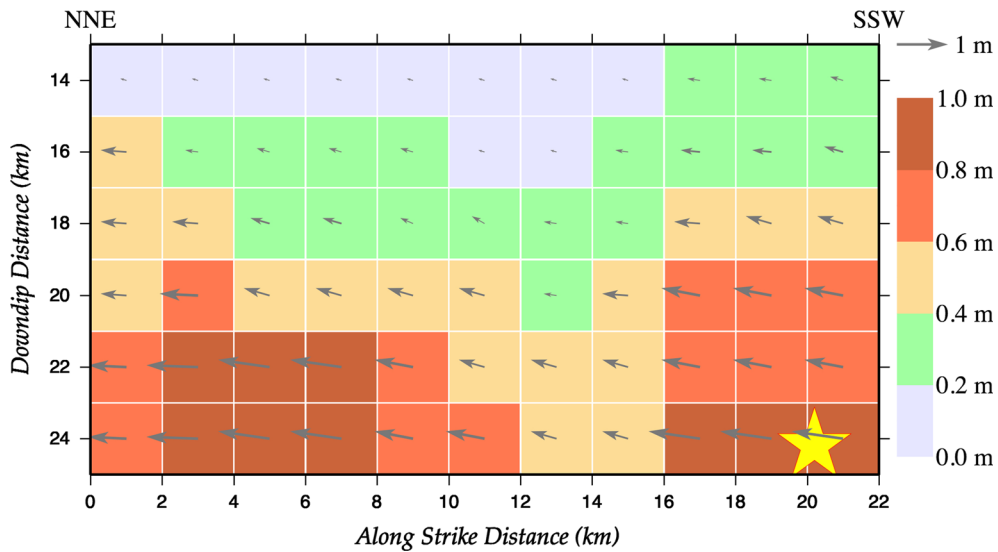
Figure 10
Variable slip *rectangular* fault model

10 mm for uplift, 8.7 mm northwards, and 1.7 westwards, they appear almost identical with our calculated values (9.7 mm uplift—8.5 mm northward—1.5 mm westwards).

The displacement field calculated by the PS technique resembles the one calculated from the variable slip model identified in this study, exhibiting uplift to the NW and SE of the main fault and subsidence to the SW and NE. The displacement field calculated by the PS technique resembles the one calculated from the variable slip model defined in this study. The validity of the model results is examined by the calculation of their differences from the ones obtained by the PS technique. The map distribution of Fig. 12a shows a 15-km-wide NE–SW trending zone along the trace of the fault plane with differences between the variable slip model and the PS technique, less than 5 mm. The most significant differences are observed along the NE–SW trending coastal zone. The geodetic data show high subsidence while the model predicts uplift or weak subsidence. This disagreement might be attributed to the properties of the unconsolidated sediments that cover the coastal area. The resulted by PS technique uplift east to northeast of the main rupture, which disagrees with the subsidence predicted by the model, is probably influenced by the

activation of adjacent fault segments. There is, however, lack of adequate data that are necessary for a deeper insight. The robustness of the proposed variable model in relation to a homogeneous one is examined by the calculation of the differences between the results of a homogeneous slip model and the geodetic technique (Fig. 12b). Comparison of the two maps reveals that the displacement field that was calculated according to the variable slip model exhibits a rather broad zone around the main fault with differences less than 5 mm from the mean values of PSI data, which have a scattering of the same order or larger.

4.4. Calculation of Static Stress Changes

The calculation of the static Coulomb stress changes associated with the coseismic slip of the main rupture is benefited from the variable slip model and fault dimensions specified from significantly improved aftershock relocation, which constitute the input information. The Poisson's ratio and shear modulus are taken equal to 0.25 and 33 GPa, respectively, the latter being assigned the same value as in the deformation field calculations presented above. A friction coefficient equal to $\mu = 0.75$ and a Skempton's coefficient equal to $B = 0.5$ were
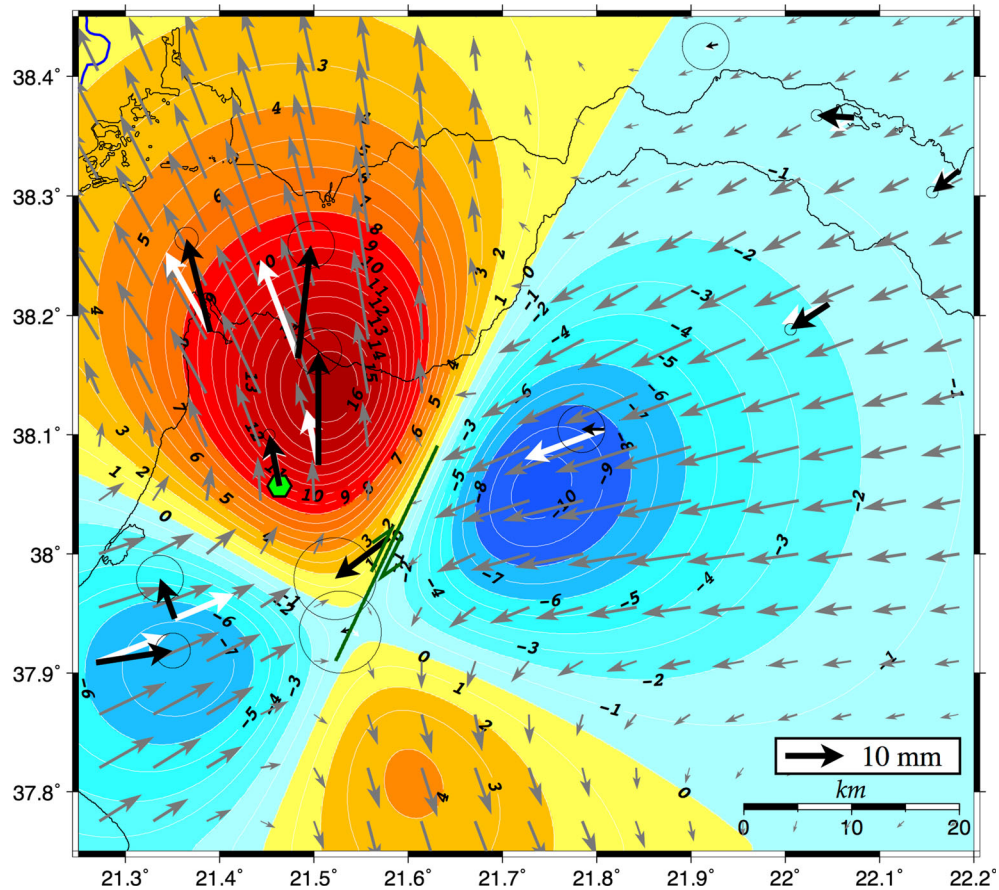
Figure 11
Calculated surface deformation field based on the variable slip model. *Vertical* (denoted by *colors*, *red* is uplift) and horizontal (denoted by *arrows*) displacements are shown. GPS station RLS is marked as a *green hexagon*. *White* and *black arrows* show horizontal displacements calculated with our model and published by Serpetsidaki et al. (2014), respectively

assumed, which result in an apparent coefficient of friction $\mu' = 0.4$, the value suggested by Papadimitriou (2002) after testing the appropriateness of different μ' values for the central Ionian area. Stress changes were calculated at a depth of 20 km and according to the main shock faulting type.

Figure 13 demonstrates that the stress-enhanced areas encompass mainly the seismicity associated with the southward extension of the fault zone, and minor clusters inside the western and eastern lobes. Onto-fault aftershocks are located inside the slipped zone and consequently the area of negative stress changes. A drawback of our calculations is that the activity beyond the northern edge of the fault, unlike the one in the southern part, was not found inside a

stress-enhanced area. Taking into account that the stress tensor is spatially variable according to the fault orientation and slip, it is expected that stress changes distribution will become different when they will be resolved for different faulting types.

The next step is then to investigate whether ΔCFF calculations resolved according to the geometry and sense of slip of the active structure associated with the northern cluster, might explain triggering at that place. For quantifying such correlation, the static stress change at the focus of each aftershock belonging to the northern cluster, and in particular located northern than 38.09° north latitude, was calculated for three different cases. Firstly, calculations were performed for the main rupture faulting type (205/83/
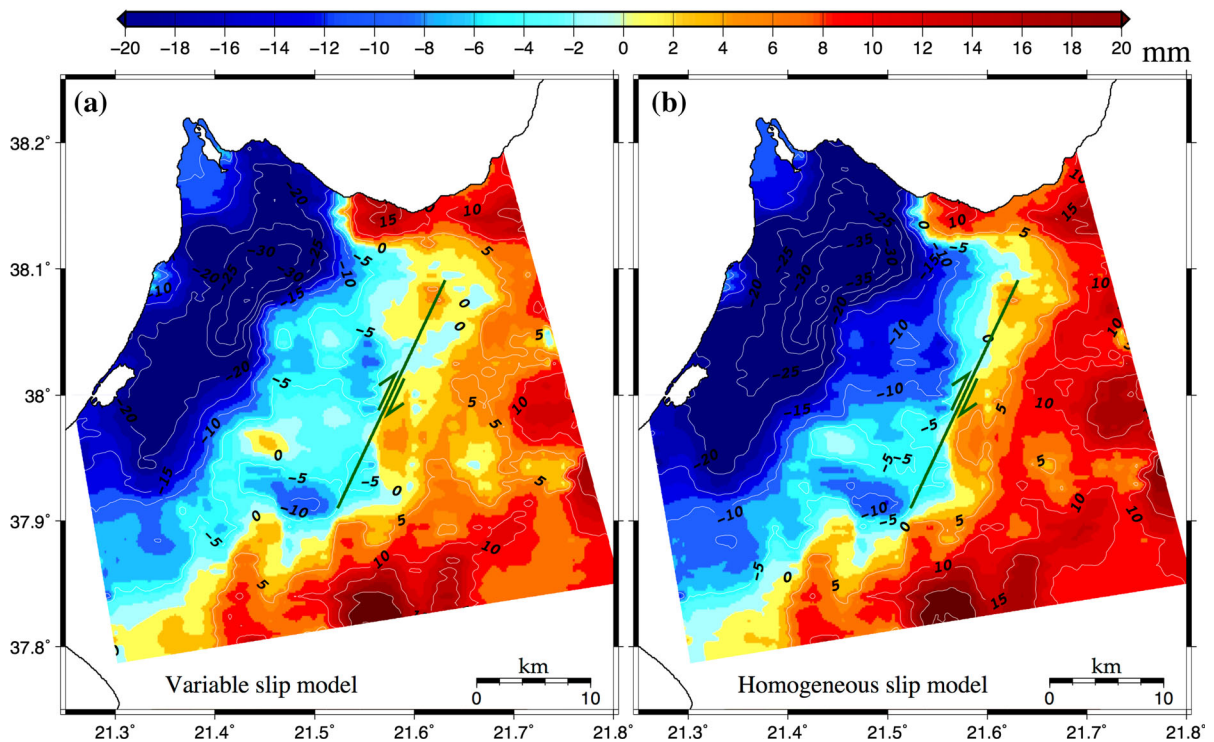
Figure 12
Differences in surface deformation map (in LOS direction) for coseismic period, according to the variable slip model (**a**) and the homogeneous slip model (**b**)

164) and the values of the calculated static stress changes are shown as a frequency histogram in Fig. 14a, where the positive and negative ones, are shown in red and blue color, respectively. The prevalence of the negative ΔCFF values is evident with 834 earthquakes (70.08 %) located inside negative instead of 356 (29.92 %) ones located inside positive lobes. The fault geometry identified in strike-parallel and strike-normal cross sections shown in Fig. 7 is now considered for inverting the stress field, namely a strike = 240° for a vertical fault plane. Assuming the principal stress orientation as in the main rupture, a slip angle of −120° was calculated. The number of earthquakes originating in stress-enhanced areas is now more than twice the ones located in stress shadow, and particularly 847 (71.18 %) instead of 343 (28.82 %), respectively (Fig. 14b). For substantiating the robustness of the latter results, one more test was carried out by considering a strike of 295°, in accordance with the clusters found by Serpetsidaki et al. (2014), which

now requires a slip angle of −105°. Possible triggering is again evidenced with 743 (62.44 %) against 447 (37.56 %) events assigned positive and negative stress changes, respectively (Fig. 14c); however, in lesser degree than in the case where the faulting geometry identified in this study was assumed.

5. Temporal Variation of the b value

The abundance of data and the period of more than 6.5 years that they cover, permit a quantitative seismicity analysis in the study area, aiming to deduce properties of the seismic sequence. As mentioned above, the seismic excitation was extended in an elongated area of more than 50 km in length. Given that the target focuses at the main fault properties, the aftershocks that are located across the main fault are only taken into account in the analysis. We followed the approach of Zhang et al. (2015) who analyzed the 2008 Wenchuan aftershock sequence
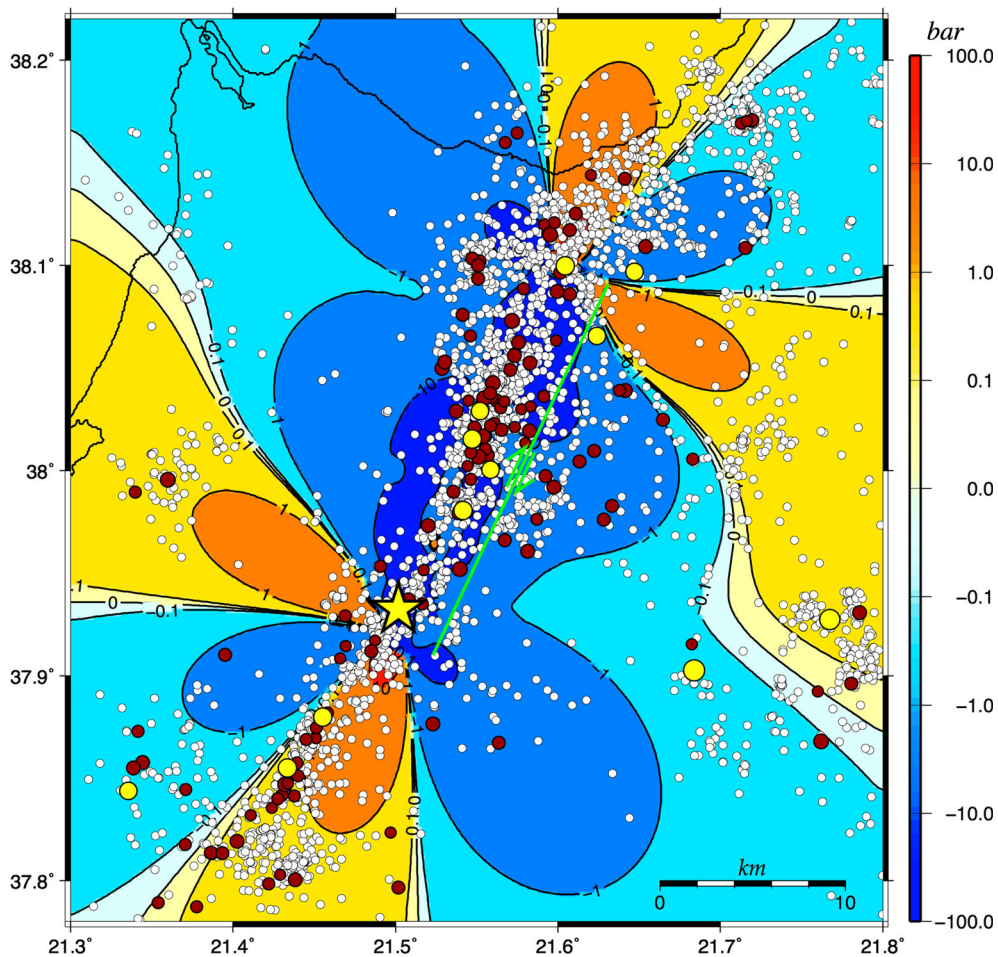
Figure 13

Map view of the Coulomb stress changes resolved according to the main shock faulting type at a depth of 20 km. Changes are denoted by the *color scale* to the *right* (in *bars*) and by *numbers* on the *contour lines*. The main shock epicenter is depicted by the *star* and the ones of aftershocks by *circles*, the *color* and *size* of which is scaled according to magnitude, similarly to Fig. 3. The inferred fault trace is shown by the *green line*

and determined the apparent healing time of the fault from the temporal variation of the *b* value. They specified this time to be the time since when the *b* value was stabilized after exhibiting an increasing trend since the main shock occurrence.

For the *b* value calculation complete data samples are sine qua non. In the case of seismic sequences the completeness varies with time and needs to be treated with caution. Soon after the main shock and in particular in the first hours and days, smaller magnitude aftershocks are overshadowed by the more frequent larger aftershocks. The completeness magnitude, M_c, is found larger in the

first days than afterwards. For the above explained reason the magnitude completeness was thoroughly sought throughout the period that our data cover. The aftershock catalog is divided into three subcatalogs covering three time intervals, namely, the first subset includes earthquakes that occurred during 08/06/2008–31/12/2008, the second during 2009–2011 and the third one during 2012–2014. The completeness magnitude, M_c, in each subcatalog was identified by applying the formulation of Wiemer and Wyss (2000). The M_c was found equal to 2.3, 2.0 and 1.6, for the first, second and third interval, respectively.
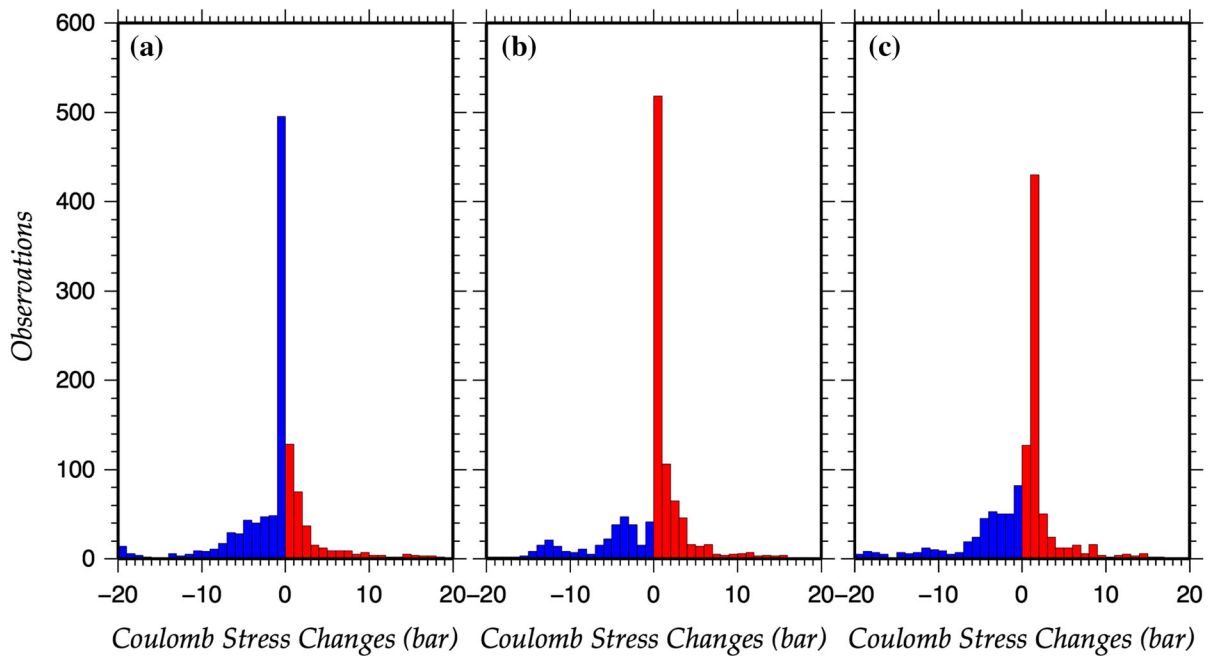
Figure 14
Histograms of Coulomb stress changes resolved at the focus of each earthquake occurred northern than 38.09° beyond the tip of the main fault. Positive and negative changes are depicted in *red* and *blue color*, respectively. Frequency histograms of static stress changes calculated according to **a** the main rupture faulting type, **b** the faulting type assigned to the northern cluster in this study, and **c** with a strike of 295°

In each subcatalog successive subsets of 40 events were created by replacing and moving 5 events at each step. The main shock was not included in the first subset, which started with the aftershock that occurred on 08/06/2008 at 12:40:53.70 with $M = 3.9$. The b value was calculated for each subset with the relation (Aki 1965):

$$b = \frac{\log e}{M_{mean} - M_{min}}, \qquad (1)$$

where M_{mean} and M_{min} are the mean and minimum magnitude, respectively. In our case this latter corresponds to the M_c of the subcatalog to which the subset belongs.

The temporal variation of the b value is presented in Fig. 15 and for three different periods for detailing the fluctuations since at the beginning the samples are considerably denser in time. The first 700 days of the study period are shown because they are adequate to demonstrate that the b value attains values 1.0–1.1 for at least the half of this time (between ~ 320 and 700th day, Fig. 15a). The gap in data between ~ 20

and 200 days, implies that the on-fault seismicity ceased, one first indication of rapid fault healing. For quantifying this observation the b values are shown during the first 20 days in Fig. 15b. In the first 3 days they show an increasing trend with values up to 1.4 and then, on the 9th day approximately, they stabilized very close to 1.0. The persistent increase in the first 3 days is better shown in Fig. 15c, since the beginning of the sequence with very low b values (~ 0.50).

6. Discussion and Conclusions

The aftershock sequence of the 8 June 2008 earthquake provided the opportunity to investigate an area which has not been known that has struck in strong ($M \geq 6.0$) events before. The activity that remained high for years afterwards was recorded by a sufficient number of seismological stations located at distances that secure the location accuracy. The advantage of this study in comparison with the
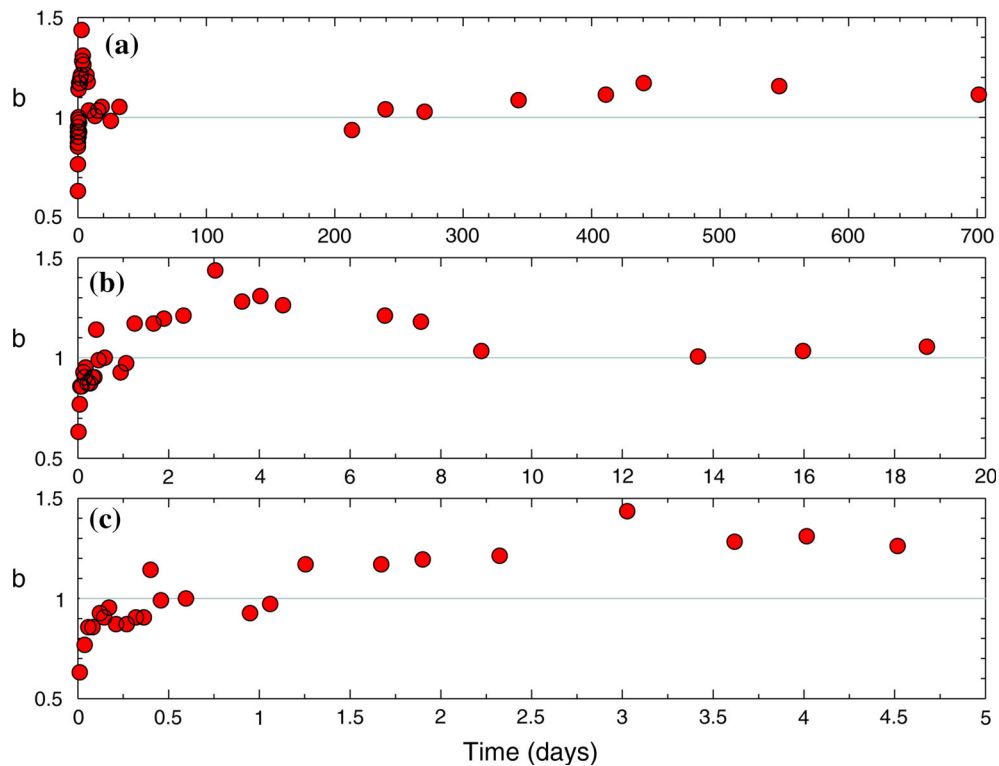
Figure 15
Variation of b values as a function of time given in days since the main shock occurrence for three different time intervals, **a** the entire study period of more than 6.5 years, **b** the first 20 days when the b parameter seems to attain stable value and **c** for the first 5 days when the b values showed an increasing trend

previous ones (Konstantinou et al. 2009; Serpetsidaki et al. 2014) is that a much larger number of after-shocks (a few thousands instead of a few hundreds), for much longer period (years instead of weeks) and with exhaustive efforts for improving locations (a specific velocity model, stations delays in addition to HYPOINVERSE, double difference and cross-corre-lation techniques). The location uncertainties are attained to get diminutive values, supporting identi-fication of the fine details of the activated area. The main rupture position in 3-D representation, its dimensions and geometrical properties, possible asperities, activation of other small faults around the main one, were revealed because of data abundance and accuracy.

The orientation of the aftershock spatial distribu-tion manifests a fault striking NNE–SSW, in accordance with the dextral strike–slip faulting sug-gested by the GCMT solution. Spatial clusters, able to

be discerned, are associated with adjacent fault seg-ments being triggered by the coseismic slip of the main rupture, as it has been shown after calculating the static stress changes for appropriate faulting type. Seismicity is constrained to depths 10–30 km, implying an upper stability transition at 10 km of unconsolidated surface crustal layer. This thickness of the upper stable crustal layer was observed in the investigation of the 1993 Patras earthquake, where aftershock depths were estimated at 14–22 km (Karakostas et al. 1994).

The main fault and its southwestward continua-tion with a slightly different strike, are positioned at a high angle to the almost E–W striking Corinth rift to the north and the NW–SE striking subduction front to the west, both constituting major locations of active deformation and consequently expressions of the dominant stress field. The dextral strike–slip motion and orientation perfectly agrees with the Kefalonia

Transform Fault Zone (KTFZ) located to the north-west. It is premature to dare any local geodynamic model for interpreting the activated structure, which is nevertheless concordant to the stress field, with almost NNW–SSE extension and ENE–WSW compression axis orientation. The faulting complexity and the location and geometry of the faults capable of failing in strong earthquakes need additional data and careful analysis of continuous seismicity, for becoming adequate for seismic hazard evaluation.

For disclosing a comprehensive description, the seismicity analysis findings are associated with surface displacements imaged from InSAR time series techniques. The Stanford Method for Persistent Scatterers (StaMPS) was used to calculate the deformation field at the location and adjacent area of the main rupture from SAR data. The coseismic deformation is concentrated in "patches" near the fault, with uplift to the north–west and south–east part of fault, and subsidence to the south–west and north–east. The PS deformation when compared with geodetic measurements from a nearby GPS station (Ganas et al. 2009) was found to be in good agreement. Coseismic displacement observed on the GPS station is 10.53 ± 0.85 mm in the vertical component (uplift) while displacement for PS points near the GPS station is about 7.5 mm (uplift).

The 3-D representation of the main fault based on the satisfactorily accurate aftershock locations and the comparison between the surface deformation calculated for an elastic dislocation with a uniform coseismic slip with the PS deformation field, helped to the construction of a variable slip model, which better approaches the geodetic observations than a fault model with constant slip. Coulomb stress changes adequately explain the southwest prolongation of the off-fault activity during the study period. The activity beyond the northern main fault edge was also shown to be triggered, when the static stress field changes are resolved for the faulting type of this active structure. This conclusion was drawn after the prevalence of hypocenters with stress-enhanced locations. The relocated aftershocks were increased from ∼29.92 to 71.18 % when the stress field was resolved for the faulting type of the fault zone where from they were originated.

Regarding the healing process which has been examined through the temporal variation of b values, it came out that the fault has gained its pre-seismic strength very quickly in a few days. Since the healing prevents postseismic activity, this is in accordance with the paucity of seismicity onto the main fault segment. Although the healing rate is larger in the earlier stage after the earthquake, indicated by the wide range of b values of about 1 unit in the first 3 days, the stabilization close to 1.0 after the 9th day is unambiguous. This indication along with the results of Zhang et al. (2015) need to be enriched and compared with several cases before being accepted as decisive for fault healing time identification.

REFERENCES

Aki, K. (1965). Maximum likelihood estimate of b in the formula logN = a–bm and its confidence limits. *Bulletin of the Earthquake Research Institute University, 43*, 137–139.

Ambraseys, N. (2009). *Earthquakes in the Mediterranean and Middle East: a multidisciplinary study of seismicity up to 1900.* Cambridge: Cambridge University Press.

Armijo, R., Meyer, B., King, G. C. P., Rigo, A., & Papanastassiou, D. (1996). Quaternary evolution of the Corinth Rift and its implications for the late Cenozoic evolution of the Aegean. *Geophysical Journal International, 126*, 11–53.

Bath, M. (1965). Lateral inhomogeneities of the upper mantle. *Tectonophysics, 2*, 483–514.

Beeler, N. M., Simpson, R. W., Hickman, S. H., & Lockner, D. A. (2000). Pore fluid pressure, apparent friction and Coulomb failure. *Journal Geophysical Research, 105*, 25533–25542.

Bernard, P., Lyon-Caen, H., Briole, P., Deschamps, A., Boudin, F., Makropoulos, K., et al. (2006). Seismicity, deformation and seismic hazard in the western rift of Corinth: new insights from the Corinth Rift Laboratory (CRL). *Tectonophysics, 426*, 7–30.

Console, R., Falcone, G., Karakostas, V., Murru, M., Papadimitriou, E., & Rhoades, D. (2013). Renewal models and coseismic stress transfer in the Corinth Gulf, Greece, fault system. *Journal of Geophysical Research: Solid Earth, 118*, 3655–3673. doi:10.1002/jgrb.50277.

Deng, J., & Sykes, L. (1997). Evolution of the stress field in Southern California and triggering of moderate size earthquakes: a 200-year perspective. *Journal Geophysical Research, 102*, 9859–9886.

Drakatos, G., & Latoussakis, J. (2001). Some features of aftershock patterns in Greece. *Geophysical Journal International, 126*, 123–134.

Erikson, L. (1986). User's manual for DIS3D: A three-dimensional dislocation program with applications to faulting in the Earth. Master Thesis, Stanford University, Stanford, California, pp. 167.

Feng, L., Newman, A. V., Farmer, G. T., Psimoulis, P., & Stiros, S. (2010). Energetic rupture, coseismic and post-seismic response of the 2008 Mw6.4 Achaia-Elia earthquake in northwestern Peloponnese, Greece: an indicator of an immature transform fault. *Geophysical Journal International, 183*, 103–110.

Ferretti, A., Prati, C., & Rocca, F. (2000). Nonlinear subsidence rate estimation using permanent scatterers in differential SAR interferometry. *IEEE Transactions on Geoscience and Remote Sensing, 38*, 2202–2212.

Ferretti, A., Prati, C., & Rocca, F. (2001). Permanent scatterers in SAR interferometry. *IEEE Transactions on Geoscience and Remote Sensing, 39*, 8–20.

Gallovič, F., Zahradnik, J., Křižová, D., Plicka, V., Sokos, E., Serpetzidaki, A., Tselentis, G. A. (2009). From earthquake centroid to spatial-temporal rupture evolution: $M_w6.3$ Movri Mountain earthquake, June 8, 2008, Greece. *Geophysical Research Letters, 36*, L21310. doi:10.1029/2009GL040283.

Ganas, A., Serpelloni, E., Drakatos, G., Kolligri, M., Adamis, I., Tsimi, Ch., et al. (2009). The M_w 6.4 SW-Achaia (western Greece) earthquake of 8 June 2008: seismological, field, GPS observations, and stress modeling. *Journal of Earthquake Engineering, 13*, 1101–1124.

Geller, R. J., & Mueller, C. S. (1980). Four similar earthquakes in central California. *Geophysical Reseach Letters, 7*, 821–824.

Giannopoulos, D., Sokos, E., Konstantinou, K., Lois, A., & Tsalentis, G. A. (2012). Temporal variations of shear-wave splitting parameters before and after the 2008 Movri Mountain earthquake in northwest Peloponnese (Greece). *Annals of geophysics, 55*, 1027–1038. doi:10.4401/ag-5586.

Harris, R. A. (1998). Introduction to special section: stress triggers, stress shadows, and implications for seismic hazard. *Journal Geophysical Research, 103*, 24347–24358.

Haslinger, F., Kissling, E., Ansorge, J., Hatzfeld, D., Papadimitriou, E., Karakostas, V., et al. (1999). 3D crustal structure from local earthquake tomography around the gulf of Arta (Ionian region, NW Greece). *Tectonophysics, 304*, 201–218.

Hollenstein, Ch., Muller, M. D., Geiger, A., & Kahle, H. G. (2008). Crustal motion and deformation in Greece from a decade of GPS measurements, 1993–2003. *Tectonophysics, 449*, 17–40.

Hooper, A., Segall, P., & Zebker, A. (2007). Persistent scatterer interferometric synthetic aperture radar for crustal deformation analysis, with application to Volcán Alcedo. *Journal of Geophysical Research: Solid Earth, 112*, B07407. doi:10.1029/2006JB004763.

Hooper, A., Zebker, H., Segall, P., & Kampes, B. (2004). A new method for measuring deformation on volcanoes and other natural terrains using InSAR persistent scatterers. *Geophysical research letters, 31*, L23611. doi:10.1029/2004GL021737.

http://www.nrcan.gc.ca/earth-sciences/geomatics/satellite-imagery-air-photos/satellite-imagery-products/educational-resources/9325

Hutton, L. K., & Boore, D. M. (1987). The M_L scale in southern California. *Bulletin of the Seismological Society of America, 77*, 2074–2094.

Karakostas, V., Karagianni, E., & Paradisopoulou, P. (2012). Space-time analysis, faulting and triggering of the 2010 earthquake doublet in western Corinth Gulf. *Natural Hazards, 63*, 1181–1202.

Karakostas, B. G., Karakaisis, G. F., Papaioannou, Ch. A., Baskoutas, J., Drakopoulos, J., Papazachos, B. C. (1993b). Preliminary study of the focal properties of the Pyrgos, 1993 earthquake (NW Peloponnesus–Greece). In *2nd Congress Hellenic Geophysical Union, Florina, 5–7 May 1993* (pp. 418–426).

Karakostas, V., Papadimitriou, E., & Gospodinov, D. (2014). Modelling the 2013 North Aegean (Greece) seismic sequence: geometrical and frictional constraints, and aftershock probabilities. *Geophysical Journal International, 197*, 525–541. doi:10.1093/gji/ggt523.

Karakostas, B. G., Papadimitriou, E. E., Hatzfeld, D., Makaris, D. I., Makropoulos, K. C., Diagourtas, D., et al. (1994). The aftershock sequence and focal properties of the July 14, 1993 (Ms = 5.4) Patras earthquake. *Bulletin of the Geological Society of Greece, XXX/5*, 167–174.

Karakostas, V. G., Papadimitriou, E. E., Karakaisis, G. F., Papazachos, C. B., Scordilis, E. M., Vargemezis, G., et al. (2003). The 2001 Skyros, northern Aegean, Greece, earthquake sequence: off fault aftershocks, tectonic implications and seismicity triggering. *Geophysical Reseach Letters, 30*(1), 1012. doi:10.1029/2002GL015814.

Karakostas, B. G., Scordilis, E. M., Papaioannou, Ch. A., Papazachos, B. C., Mountrakis, D. (1993a). Focal properties of the October 16, 1988 Killini earthquake (western Greece). In *2nd Congress Hellenic Geophysical Union, Florina, 5–7 May 1993* (pp. 136–145).

King, G. C. P., Stein, R. S., & Lin, J. (1994). Static stress changes and the triggering of earthquakes. *Bulletin of the Seismological Society of America, 84*, 935–953.

Kiratzi, A., Sokos, E., Ganas, A., Tselentis, G., Benetatos, C., Roumelioti, Z., et al. (2008). The April 2007 earthquake swarm near Lake Trichonis and implications for active tectonics in western Greece. *Tectonophysics, 452*, 51–65.

Kissling, E., Ellsworth, W. L., Eberhart–Phillips, D., & Kradolfer, U. (1994). Initial reference models in local earthquake tomography. *Journal Geophysical Research,*. doi:10.1029/93JB03138.

Klein, F. W. (2000). *User's Guide to HYPOINVERSE–2000, a Fortran program to solve earthquake locations and magnitudes.* US Geological Survey. Open File Report 02–171 Version 1.0.

Konstantinou, K. I., Melis, N. S., Lee, S. J., Evangelidis, C. P., & Boukouras, K. (2009). Rupture process and aftershock relocation of the 8 June 2008 M_w6.4 earthquake in northwest Peloponnese, western Greece. *Bulletin of the Seismological Society of America, 99*, 3374–3389. doi:10.1785/0120080301.

Koukouvelas, I., Kokkalas, S., & Xypolias, P. (2010). Surface deformation during the M_w6.4 (8 June 2008) Movri Mountain earthquake in the Peloponnese, and its implications for the seismotectonics of western Greece. *International Geology Review, 52*, 249–268.

Margaris, B., Athanasopoulos, G., Mylonakis, G., Papaioannou, Ch., Klimis, N., Theodulidis, N., et al. (2010). The 8 June 2008 Mw6.5 Achia-Elia, Greece earthquake: source characteristics, ground motions, and ground failure. *Earthquake Spectra, 26*, 399–424.

McKenzie, D. P. (1972). Active tectonics of the Mediterranean region. *Geophysical Journal of the Royal Astronomical Society, 30*, 109–185.

Melis, N., & Tselentis, G. A. (1998). 3–D P–wave velocity structure in western Greece determined from tomography using earthquake data recorded at the University of Patras seismic network (PATNET). *Pure and Applied Geophysics, 152*, 329–348.

Mirek, K., Papadimitriou, E., Karakostas, V., Mirek, J. (2012). Coseismic surface displacement study of Achaia–Elia earthquake—preliminary results. In *33rd General Assembly of European Seismological Commission, Moscow, 19–24 August 2012*.

Novotny, O., Jansky, J., Plicka, V., & Lyon–Caen, H. (2008). A layered model of the upper crust in the Aigion region of Greece, inferred from arrival times of the 2001 earthquake sequence. *Studia Geophysica et Geodaetica, 52*, 123–131.

Okada, Y. (1992). Internal deformation due to shear and tensile faults in a half–space. *Bulletin of the Seismological Society of America, 82*, 1018–1040.

Paige, C., & Saunders, M. (1982). LSQR: an algorithm for sparse linear equations and sparse least squares. *ACM Transactions on Mathematical Software, 8*, 43–71.

Papadimitriou, E. E. (2002). Mode of strong earthquake recurrence in central Ionian Islands (Greece) Possible triggering due to Coulomb stress changes generated by the occurrence of previous strong shocks. *Bulletin of the Seismological Society of America, 92*, 3293–3308.

Papadopoulos, G., Karastathis, V., Kontoes, Ch., Charalampakis, M., Fokaefs, A., & Papoutsis, I. (2010). Crustal deformation associated with east Mediterranean strike-slip earthquakes: the 8 June 2008 Movri (NW Peloponnese), Greece, earthquake (M_w6.4). *Tectonophysics, 492*, 201–212.

Papazachos, B. C., & Comninakis, P. E. (1971). Geophysical and tectonic features of the Aegean Arc. *Journal Geophysical Research, 76*, 8517–8533.

Papazachos, B. C., & Papazachou, C. C. (2003). *The earthquakes of Greece*. Ziti Publication Co.

Papazachos, B. C., Scordilis, E. M., Panagiotopoulos, D. G., Papazachos, C. B., Karakaisis, G. F. (2004). Global relations between seismic fault parameters and moment magnitude of earthquakes. In *10th International Congress of the Hellenic Geographical Society, Thessaloniki, Greece, 14–17 April 2004* (pp. 539–540).

Pavlides, S., Papathanassiou, G., Valkaniotis, S., Chatzipetros, A., Sboras, S., Caputo, R. (2013). Rock–falls and liquefaction related phenomena triggered by the June 8, 2008, $M_w = 6.4$ earthquake

in NW Peloponnesus, Greece. *Annals of Geophysics, 56*, S0682, doi:10.4401/ag-5807.

Rice, J., & Cleary, M. (1976). Some basic stress diffusion solutions for fluid saturated elastic porous media with compressible constituents. *Reviews of Geophysics, 14*, 227–241.

Richards-Dinger, K., Stein, R. S., & Toda, S. (2010). Decay of aftershock density with distance does not indicate triggering by dynamic stress. *Nature, 467*, 583–588. doi:10.1038/nature09402.

Rigo, A., Lyon-Caen, H., Armijo, R., Deschamps, A., Hatzfeld, D., Makropoulos, K., et al. (1996). A micro-seismic study in the western part of the Gulf of Corinth (Greece): implications for large-scale normal faulting mechanisms. *Geophysical Journal International, 126*, 663–688.

Roumelioti, Z., Benetatos, Ch., Kiratzi, A., Stavrakakis, G., & Melis, N. (2004). A study of the 2 December 2002 (M5.5) Vartholomio (western Peloponnese, Greece) earthquake and of its largest aftershocks. *Tectonophysics, 387*, 65–79.

Roumelioti, Z., Theodoulidis, N., & Bouchon, M. (2013). Constraints on the location of the 2008, Mw6.4 Achaia–Ilia earthquake fault from strong motion data. *Bulletin Geological Society Greece, XLVII*, 10.

Schaff, D. P., Bokelmann, G. H. R., Ellsworth, W. L., Zanzerkia, E., Waldhauser, F., & Beroza, G. C. (2004). Optimizing correlation techniques for improved earthquake location. *Bulletin of the Seismological Society of America, 94*, 705–721.

Schaff, D. P., & Waldhauser, F. (2005). Waveform cross-correlation-based differential travel–time measurements at the northern California seismic network. *Bulletin of the Seismological Society of America, 95*, 2446–2461.

Scordilis, E. M., Karakaisis, G. F., Karakostas, B. G., Panagiotopoulos, D. G., Comninakis, P. E., & Papazachos, B. C. (1985). Evidence for transform faulting in the Ionian Sea: the Cephalonia Island earthquake sequence. *Pure and Applied Geophysics, 123*, 388–397.

Serpetsidaki, A., Elias, P., Ilieva, M., Bernard, P., Briole, P., Deschamps, A., et al. (2014). New constraints from seismology and geodesy on the $M_w = 6.4$ 2008 Movri (Greece) earthquake: evidence from growing strike–slip fault system. *Geophysical Journal International, 198*, 1373–1386.

Stein, R. (1999). The role of stress transfer in earthquake occurrence. *Nature, 402*, 605–609.

Stiros, S., Moschas, F., Feng, L., & Newman, A. (2013). Long-term versus short-term deformation of the meizoseismal area of the 208 Achaia-Elia (Mw6.4) earthquake in NW Peloponnese, Greece: evidence from historical triangulation and morphotectonic data. *Tectonophysics, 592*, 150–158.

Stramondo, S., Moro, M., Tolomei, C., Cinti, F. R., & Doumaz, F. (2005). InSAR surface displacement field and fault modeling for the 2003 Bam earthquake (southeastern Iran). *Journal of Geodynamics, 40*, 347–353.

Vassilakis, E., Royden, L., & Papanikolaou, D. (2011). Kinematic links between subduction along the Hellenic trench and extension in the Gulf of Corinth, Greece: a multidisciplinary analysis. *Earth and Planetary Science Letters, 303*, 108–120.

Waldhauser, F. (2001). *HypoDD—a program to compute double-difference hypocenter locations*. US Geological Survey Open File Report, pp. 01–113.

Waldhauser, F., & Ellsworth, W. L. (2000). A double-difference earthquake location algorithm: method and application to the Northern Hayward Fault, California. *Bulletin of the Seismological Society of America, 90*, 1353–1368.

Walters, R. J., Elliot, J. R., D' Agostino, N., England, P. C., Hunstad, I., Jackson, J. A., et al. (2009). The 2009 L'Aquila earthquake (central Italy): a source mechanism and implications for seismic hazard. *Geophysical Reseach Letters, 36,* L17312. doi:10.1029/2009GL039337.

Wells, D. L., & Coppersmith, K. J. (1994). New empirical relationships among magnitude, rupture length, rupture width, rupture area, and surface displacement. *Bulletin of the seismological Society of America, 84,* 974–1002.

Wessel, P., & Smith, W. H. F. (1998). New, improved version of the Generic Mapping Tools Released. *Eos, Transactions American Geophysical Union, 79,* 579.

Wiemer, S., & Wyss, M. (2000). Minimum magnitude of completeness in earthquake catalogs: examples from Alaska, the Western United States, and Japan. *Bulletin of the Seismological Society of America, 90,* 859–869.

Zahradnik, J., & Gallovic, F. (2010). Toward understanding slip inversion uncertainty and artifacts. *Journal Geophysical Research, 115,* B09310. doi:10.1029/2010JB007414.

Zhang, S., Wu, Z., & Jiang, C. (2015). *Signature of fault healing in an aftershock sequence? The 2008 Wenchuan earthquake*. Pure Appl: Geophys. doi:10.1007/s00024-015-1086-x.

Zygouri, V., Koukouvelas, I. K., Kokkalas, S., Xypolias, P., & Papadopoulos, G. A. (2015). The Nisi fault as a key structure for understanding the active deformation of the NW Peloponnese, Greece. *Geomorphology, 237,* 142–156.